Global linear stability analysis of the wake and path of buoyancy-driven disks and thin cylinders

Joël Tchoufag, David Fabre, Jacques Magnaudet

Global linear stability analysis of the wake and path of buoyancy-driven disks and thin cylinders

Joël Tchoufag[1], David Fabre[1] and Jacques Magnaudet[1,2,†]

[1]Université de Toulouse, INPT, UPS, IMFT (Institut de Mécanique des Fluides de Toulouse), Allée Camille Soula, F-31400 Toulouse, France

[2]CNRS, IMFT, F-31400 Toulouse, France

The stability of the vertical path of a gravity- or buoyancy-driven disk of arbitrary thickness falling or rising in a viscous fluid, recently studied through direct numerical simulation by Auguste, Magnaudet & Fabre (*J. Fluid Mech.*, vol. 719, 2013, pp. 388–405), is investigated numerically in the framework of global linear stability. The disk is allowed to translate and rotate arbitrarily and the stability analysis is carried out on the fully coupled system obtained by linearizing the Navier–Stokes equations for the fluid and Newton's equations for the body. Three disks with different diameter-to-thickness ratios are considered: one is assumed to be infinitely thin, the other two are selected as archetypes of thin and thick cylindrical bodies, respectively. The analysis spans the whole range of body-to-fluid inertia ratios and considers Reynolds numbers (based on the fall/rise velocity and body diameter) up to 350. It reveals that four unstable modes with an azimuthal wavenumber $m = \pm 1$ exist in each case. Three of these modes result from a Hopf bifurcation while the fourth is associated with a stationary bifurcation. Varying the body-to-fluid inertia ratio yields rich and complex stability diagrams with several branch crossings resulting in frequency jumps; destabilization/restabilization sequences are also found to take place in some subdomains. The spatial structure of the unstable modes is also examined. Analyzing differences between their real and imaginary parts (which virtually correspond to two different instants of time in the dynamics of a given mode) allows us to assess qualitatively the strength of the mutual coupling between the body and fluid. Qualitative and quantitative differences between present predictions and known results for wake instability past a fixed disk enlighten the fact that the first non-vertical regimes generally result from an intrinsic coupling between the body and fluid and not merely from the instability of the sole wake.

Key words: aerodynamics, flow–structure interactions, instability

1. Introduction

Understanding and predicting the path of bodies of arbitrary shape falling/rising under gravity/buoyancy in an infinite fluid medium has always been an important concern in Mechanics, as testified by Leonardo's drawings related to the spiralling

†Email address for correspondence: magnau@imft.fr

motion of rising bubbles (Prosperetti *et al.* 2003; Prosperetti 2004). Nevertheless, despite this uninterrupted interest, robust experimental data were essentially made available within the last half-century, especially for thin disks (Willmarth, Hawk & Harvey 1964; Field *et al.* 1997).

The topic has received growing attention during the last decade for two main reasons. The first is, of course, its physical relevance and importance in many up-to-date applications such as in meteorology, ecology, bio-inspired flight, aeronautics and multiphase flows to mention just a few. The other is the growing maturity of modern observation techniques, such as high-speed video cameras and particle image velocimetry, and of three-dimensional direct numerical simulation (DNS). The latter has also become a powerful tool to explore the various non-vertical regimes of axisymmetric bodies such as freely rising spheroidal bubbles (Mougin & Magnaudet 2002*b*), falling/rising spheres (Jenny, Dusek & Bouchet 2004) and disks (Auguste, Magnaudet & Fabre 2013; Chrust, Bouchet & Dusek 2013), and determine the transitions between them, especially in the presence of strongly nonlinear effects.

Nevertheless, despite its many merits, DNS does not give a detailed access to several important aspects of the phenomena that take place near the first thresholds of the instability, such as the spatial structure of each unstable mode or the reasons that sometimes make the characteristics of path deviations (especially their geometry and frequency) change dramatically when the body geometry is slightly modified, nor does it allow the role of these various modes to be easily disentangled. Such information is better obtained by performing systematic linear or weakly nonlinear global stability analyses. This approach is also the right tool for performing parametric studies of the neutral curves corresponding to destabilization of the base flow, as DNS is very time-consuming under near-neutral conditions where the temporal transients are extremely long. However, it is only very recently that this type of approach started to be applied to this class of problems. To the best of the authors' knowledge, the first attempt is due to Assemat, Fabre & Magnaudet (2012) who carried out a systematic linear stability analysis (LSA) of the vertical path of two-dimensional bodies, such as plates and rods. Regarding three-dimensional bodies, the only work to date seems to be the weakly nonlinear analysis recently performed by Fabre, Tchoufag & Magnaudet (2012) to predict the onset and geometrical characteristics of the steady oblique (*SO*) path of spheres and disks observed under certain conditions, e.g. Veldhuis & Biesheuvel (2007) and Horowitz & Williamson (2010) for spheres.

As is now widely recognized, the presence of vorticity in the flow is at the root of path instability (as far as the body is released in such a way that no torque is created by the initial conditions), making the understanding of wake instability past the body held fixed an important prerequisite. However, this does not imply that the body dynamics are enslaved to the wake: some body paths clearly mirror the characteristics of wake modes, while other do not. Similarly, the thresholds at which these non-vertical paths set in and their oscillation frequencies often differ dramatically from those of wake instability (Alben 2008; Assemat *et al.* 2012; Auguste *et al.* 2013). These observations make it clear that any stability analysis of this class of problems must consider the body + fluid system as fully coupled, even though it may be concluded at the very end that the couplings are weak in some limit cases.

This is the essence of the present work in which we perform a systematic LSA of the entire system for a class of bodies corresponding to disks of various thicknesses which may also be thought of as thin circular cylinders. The present study is the natural extension of the work by Assemat *et al.* (2012) to axisymmetric bodies and

three-dimensional flow fields and of that by Auguste *et al.* (2013) where various falling styles of disks associated with fully nonlinear dynamics were examined using the DNS approach. The organization of the paper is as follows. The geometrical set-up, control parameters, general governing equations and main aspects of the LSA approach are described in § 2; the various operators involved in this problem and some important properties of the eigenmodes $m = 0$ and $m = \pm 1$ are made explicit in appendix B. The next three sections are devoted to the discussion of the results obtained for Reynolds numbers (based on the body diameter and rise/fall velocity) up to 350 for an infinitely thin disk and two disks with diameter-to-thickness ratios of 10 and 3, respectively. The latter two geometries are selected because available experiments (Fernandes *et al.* 2007) suggest that they may be considered as typical of the contrasting behaviours displayed by 'thin' and 'thick' bodies, respectively. Each of these sections provides some comparisons of LSA results with available DNS and experimental data and examines the contents of the stability diagrams resulting from the LSA as a function of the body-to-fluid inertia ratio. In these sections we also discuss the nature of the corresponding unstable modes and their spatial characteristics from which we show that important characteristics of the system dynamics in the fully nonlinear regime can be inferred. The paper ends with § 6 where results obtained for the three bodies are compared and physical mechanisms that make their dynamics strikingly different, especially in the limit of low inertia ratios, are discussed.

2. Problem formulation and methodological approach

2.1. *Control parameters and geometrical configuration*

We consider a three-dimensional body with uniform density and cylindrical geometry falling or rising freely under gravity in an unbounded fluid at rest at infinity. In what follows, the body which has a thickness h, diameter d and density ρ_b, will be termed a 'disk' whatever its thickness; it moves with an instantaneous velocity whose translational and rotational components are $U(t)$ and $\boldsymbol{\Omega}(t)$, respectively. The surrounding medium is a Newtonian fluid of kinematic viscosity ν and density ρ.

The problem is entirely characterized by three dimensionless parameters for which several choices are possible (Ern *et al.* 2012). The first of these is unambiguously the geometrical aspect ratio $\chi = d/h$. As a second parameter, we may choose either the body-to-fluid density ratio $\bar{\rho} = \rho_b/\rho$, or equivalently some inertia ratio I^* involving the disk's moment of inertia; the selected definition of I^* will be specified later. Note that, gravity acting downwards, 'heavy' disks such that $\bar{\rho} > 1$ fall whereas 'light' disks with $\bar{\rho} < 1$ rise. The third parameter is a 'Reynolds' number built upon the disk diameter, the viscosity and a velocity scale. Several choices are possible for the latter, as the actual disk velocity is usually not known beforehand. A possibility is to use the gravitational velocity $U_g = (2|\bar{\rho} - 1|gh)^{1/2}$, yielding the so-called Archimedes number $Ar = \sqrt{(3/32)}U_g d/\nu$. Here, we will generally make use of the velocity U_0 of the disk in the 'base state' corresponding to the steady vertical broadside motion, which yields a 'nominal' Reynolds number defined as $Re = U_0 d/\nu$. This velocity scale coincides with the actual disk's velocity as long as the deviations with respect to this base state are small, which is consistent with the linear study conducted herein. The relation between Re and Ar will be made explicit in § 2.4.

2.2. *Governing equations*

In the absolute frame of reference (O, x_0, y_0, z_0), the position of any material point of the disk may be characterized through its distance vector r from the disk's centre

of inertia C and the three angles $(\zeta, \Theta_y, \Theta_z)$ of the roll/pitch/yaw system measuring rotations in the relative or body frame (x, y, z). With these definitions one may introduce the vector $\boldsymbol{\Xi} = (\zeta, \Theta_y, \Theta_z)$ and, for small rotations, the rotation rate $\boldsymbol{\Omega} = \mathrm{d}\boldsymbol{\Xi}/\mathrm{d}t$ follows directly.

The flow around the disk of volume $\mathscr{V} = (\pi/4)d^2h$, mass $M = \rho_b \mathscr{V}$ and inertia tensor $\mathbb{I} = I_1 xx + I_2(yy + zz)$ with $I_1 = (1/8)Md^2$ and $I_2 = (1/16)Md^2(1 + (4/3\chi^{-2}))$ is described by the incompressible Navier–Stokes equations. The system of equations governing the fluid + disk dynamics is fully coupled through the fluid forces and torques acting on the disk's surface $\mathscr{S}$ on the one hand and the no-slip boundary condition on $\mathscr{S}$ imposed to the flow by the moving disk on the other hand. We express the equations in the absolute frame, but with axes rotating with the disk, following Mougin & Magnaudet (2002*a*) (the formulation adopted here differs from that employed by Assemat *et al.* (2012), where relative velocities were introduced; we checked that both formulations lead to the same results). The full set of equations reads

$$\boldsymbol{\nabla} \cdot V = 0, \tag{2.1}$$

$$\frac{\partial V}{\partial t} + (V - W) \cdot \boldsymbol{\nabla} V + \boldsymbol{\Omega} \times V = -\frac{1}{\rho}\boldsymbol{\nabla} P + \nu \nabla^2 V, \tag{2.2}$$

$$M\frac{\mathrm{d}U}{\mathrm{d}t} + M\boldsymbol{\Omega} \times U = (M - \rho\mathscr{V})g + \int_{\mathscr{S}} T \cdot n \,\mathrm{dS}, \tag{2.3}$$

$$\mathbb{I} \cdot \frac{\mathrm{d}\boldsymbol{\Omega}}{\mathrm{d}t} + \boldsymbol{\Omega} \times (\mathbb{I} \cdot \boldsymbol{\Omega}) = \int_{\mathscr{S}} r \times (T \cdot n) \,\mathrm{d}S, \tag{2.4}$$

$$\frac{\mathrm{d}\boldsymbol{\Xi}}{\mathrm{d}t} = \boldsymbol{\Omega}, \tag{2.5}$$

where $V(r, t)$ and $P(r, t)$ are the velocity and pressure fields in the fluid, $W(r, t) = U(t) + \boldsymbol{\Omega}(t) \times r$ is the local entrainment velocity, $T = -PI + \rho\nu(\boldsymbol{\nabla} V + {}^t\boldsymbol{\nabla} V)$ denotes the stress tensor and I is the Kronecker tensor. Finally, the no-slip condition on the disk surface and the vanishing of the fluid velocity at large distance imply

$$V = W \quad \text{on } \mathscr{S} \quad \text{and} \quad V = \mathbf{0} \quad \text{for } \|r\| \to \infty. \tag{2.6}$$

In the following, the governing equations and problem variables will be treated as dimensionless by normalizing lengths with d, velocities with the terminal velocity U_0 defined above, pressure and stresses with ρU_0^2, time with d/U_0 and gravity with U_0^2/d, the body mass and moments of inertia being normalized by ρd^3 and ρd^5, respectively. Instead of using the density ratio $\bar{\rho}$, we characterize the body-to-fluid relative inertia through the parameter I^* defined as the disk's dimensionless moment of inertia about one of its diameters, namely $I^* = I_2/(\rho d^5) = (\pi/64)\bar{\rho}\chi^{-1}(1 + (4/3)\chi^{-2})$. Therefore in (2.2)–(2.4), ν, M, I_1 and I_2 become Re^{-1}, $16I^*(1 + (4/3)\chi^{-2})^{-1}$, $2I^*(1 + (4/3)\chi^{-2})^{-1}$ and I^*, respectively, so that $\mathbb{I}$ is replaced by the dimensionless inertia tensor $\mathbb{I}^* = I^*\{2(1 + (4/3)\chi^{-2})^{-1}xx + yy + zz\}$.

2.3. *Strategy for the LSA and numerical implementation*

The above equations form a coupled system governing the evolution of the state vector $\boldsymbol{\mathcal{Q}} = [\boldsymbol{\mathcal{Q}}^f, \boldsymbol{\mathcal{Q}}^b]$, where $\boldsymbol{\mathcal{Q}}^f = [V(r, t), P(r, t)]$ contains the quantities associated with the fluid and $\boldsymbol{\mathcal{Q}}^b = [U(t), \boldsymbol{\Omega}(t), \boldsymbol{\Xi}(t)]$ gathers the degrees of freedom associated with the body kinematics. The latter are expressed in the moving Cartesian basis

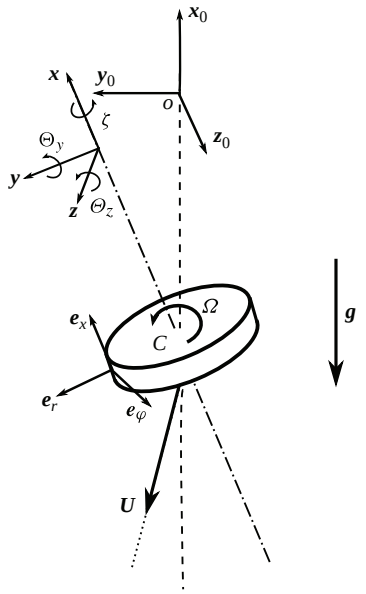

FIGURE 1. Problem configuration. The disk is assumed to be initially released with its axis oriented in the vertical direction.

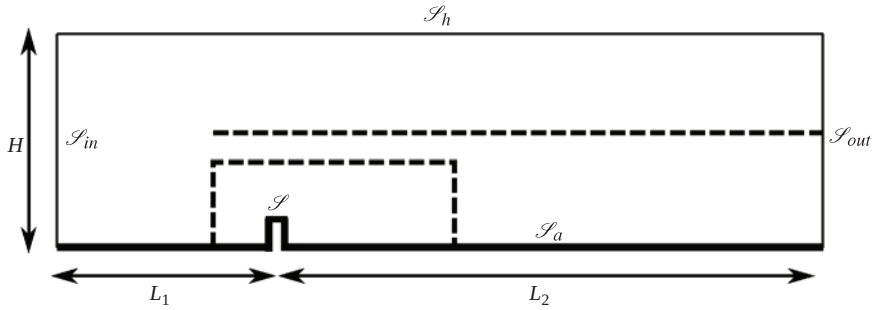

FIGURE 2. Sketch of the computational domain. Gravity g is toward the left (respectively right) for falling (respectively rising) disks.

(x, y, z) using straightforward transformations involving the roll/pitch/yaw angles (yielding for instance disk velocity components (U_x, U_y, U_z)). On the other hand, quantities associated with the fluid are projected onto the local cylindrical basis (e_r, e_φ, x) (see figure 1), yielding fluid velocity components (V_r, V_φ, V_x).

To perform the LSA of the problem, the flow is classically split into a base flow plus a disturbance in the form $\mathcal{Q} = \mathcal{Q}_0 + \epsilon q$ $(\epsilon \ll 1)$. Introducing the above ansatz in (2.5), a zeroth-order nonlinear problem and a first-order linear problem are obtained. Thanks to an azimuthal Fourier expansion of the disturbance (see below) and to symmetries detailed later, the fluid quantities only have to be computed in a two-dimensional domain corresponding to a meridional half-plane, as sketched in figure 2. We make use of the finite-element software FreeFem++ to build and invert the various matrices and of the SLPEc library to find the eigenpairs. Details regarding the weak formulation of the problem, convergence tests and boundary conditions can

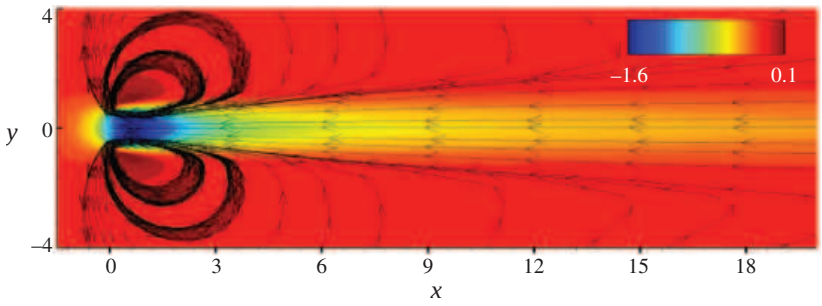

FIGURE 3. (Colour online) Example of the base flow used for the global stability analysis: case of an infinitely thin disk at $Re = 117$. The colour scale refers to the magnitude of the axial velocity; the streamlines underline the dipolar structure of the flow.

be found in appendices A and B as well as in previous related studies (Meliga, Chomaz & Sipp 2009*b*; Assemat *et al.* 2012; Tchoufag, Magnaudet & Fabre 2013).

2.4. *Base flow*

The zeroth-order (base) flow is sought in the form of a steady axisymmetric flow associated with a steady vertical broadside motion of the disk. The corresponding state vector reads merely $\mathcal{Q}_{\mathbf{0}} = [V_{\mathbf{0}}(r), P_{\mathbf{0}}(r), -x, \mathbf{0}, \mathbf{0}]$ (owing to the rotational symmetry of the body geometry, the last component of this state vector could contain an arbitrary constant angle ζ in the x direction; we set it to zero for simplicity). The associated nonlinear set of equations reads

$$\boldsymbol{\nabla} \cdot V_0 = 0, \tag{2.7}$$

$$(V_0 + x) \cdot \boldsymbol{\nabla} V_0 = -\boldsymbol{\nabla} P_0 + Re^{-1} \nabla^2 V_0, \tag{2.8}$$

It has to be supplemented by the no-slip condition $V_0 = -x_b$ on $\mathscr{S}$, the far-field condition $V_0 = \mathbf{0}$ on $\mathscr{S}_\infty \equiv \mathscr{S}_{in} \cup \mathscr{S}_h$ (see figure 2), the symmetry condition $V_{0_r} = \partial_r V_{0_x} = 0$ on the domain axis $\mathscr{S}_a$, and the zero-traction condition $-P_0 x + \rho \nu x \cdot \boldsymbol{\nabla} V_{\mathbf{0}} = \mathbf{0}$ on $\mathscr{S}_{out}$.

Figure 3 shows an example of the base flow seen in the laboratory frame in the case of an infinitely thin disk falling at a Reynolds number $Re = 117$. As one could expect, the wake structure is exactly that of the flow past a fixed disk, once the uniform flow at infinity has been removed. The drag coefficient $C_D \simeq 1.20$ compares well with the value $C_D \simeq 1.23$ determined experimentally by Roos & Willmarth (1971); the recirculation length, l_R, obtained by determining the point of the symmetry axis where $V_x = -1$, is $l_R \simeq 2.2$, in good agreement with the value $l_R \simeq 2.1$ obtained numerically for $Re = 116.9$ by Meliga, Chomaz & Sipp (2009*a*).

Although we retain the Reynolds number Re based on U_0 as one of the control parameters, comparisons with experiments have to be carried out in terms of the Archimedes number Ar defined above. The relation between Re and Ar is obtained from (2.3), which then reduces to a balance between the net weight of the disk and the drag force, namely

$$(M - \rho \mathscr{V}) g = -\int_{\mathscr{S}} T_0 \cdot n \, \mathrm{d}S \equiv -D_0 \rho d^2 U_0^2 x, \tag{2.9}$$

which in non-dimensional form leads to

$$Ar^2 = \tfrac{3}{32} Re^2 C_D(Re), \tag{2.10}$$

where $C_D = 8D_0/\pi$ denotes the dimensionless drag coefficient. This relationship holds until the threshold at which the steady vertical body motion becomes unstable is reached.

2.5. *Global mode analysis*

At order ϵ, the state vector reads $q = [v(r,t), p(r,t), u(t), \boldsymbol{\omega}(t), \boldsymbol{\xi}(t)]$ and the linearized perturbation equations take the form

$$\boldsymbol{\nabla} \cdot v = 0, \tag{2.11}$$

$$\partial_t v + (V_0 + x) \cdot \boldsymbol{\nabla} v + (v - w) \cdot \boldsymbol{\nabla} V_0 + \boldsymbol{\omega} \times V_0 = -\boldsymbol{\nabla} p + Re^{-1} \nabla^2 v, \tag{2.12}$$

$$16 \frac{I^*}{1 + \frac{4}{3}\chi^{-2}} \left\{ \frac{\mathrm{d}u}{\mathrm{d}t} - \boldsymbol{\omega} \times x \right\} - D_0(\theta_z y - \theta_y z) = \int_{\mathscr{S}} t \cdot n \, \mathrm{d}S, \tag{2.13}$$

$$\mathbb{I}^* \cdot \frac{\mathrm{d}\omega}{\mathrm{d}t} = \int_{\mathscr{S}} r \times (t \cdot n) \, \mathrm{d}S, \tag{2.14}$$

$$\frac{\mathrm{d}\xi}{\mathrm{d}t} = \omega, \tag{2.15}$$

where t is the disturbance stress tensor and θ_y and θ_z are the disturbance pitch and yaw angles, respectively. In (2.13), the last term in the left-hand side represents the $O(\epsilon)$-contribution of the net body weight; its expression is obtained by making use of (2.9) and of the projection of the gravity vector in the body frame, namely $g = -gx_0 = -gx + \epsilon g(\theta_z y - \theta_y z)$.

The system (2.11)–(2.15) must be supplemented with the no-slip condition $v = w = u + \omega \times r$ on $\mathscr{S}$, the far-field condition $v = 0$ on $\mathscr{S}_\infty$, the zero-traction condition on $\mathscr{S}_{out}$, plus suitable conditions on the symmetry axis $\mathscr{S}_a$ to be specified later.

The solution of (2.11)–(2.13) is then sought in the form of normal modes, namely

$$q = \begin{pmatrix} \hat{q}^f(r,x) \mathrm{e}^{\mathrm{i}m\varphi} \\ \hat{q}^b \end{pmatrix} \mathrm{e}^{\lambda t} + \text{c.c.}, \tag{2.16}$$

where c.c. denotes the complex conjugate, and $\lambda = \lambda_r + \mathrm{i}\lambda_i$ is the associated complex eigenvalue whose real and imaginary parts are the growth rate and frequency of the mode, respectively.

As mentioned above, the 'fluid' components $\hat{q}^f$ of the eigenvector are expressed in the local cylindrical coordinate system (r, φ, x), using the azimuthal wavenumber m to remove the φ-dependence, while the 'solid' components $\hat{q}^b$ are expressed in the Cartesian system (x, y, z).

Among the nine potential components of $\hat{q}^b = [\hat{u}, \hat{\omega}, \hat{\xi}]$, only a few have to be actually retained in the analysis. Their number depends upon the azimuthal wavenumber m. To identify the relevant components, we may consider the symmetries of the force and torque involved in the right-hand sides of (2.13) and (2.14), respectively.

(i) For $m = 0$ (axisymmetric modes), the force and torque are held by the axial direction x and hence can only be coupled to the kinematic degrees of freedom

corresponding to this direction. It is thus natural to take the corresponding solid components of the eigenmodes as $\hat{q}^b = [\hat{u}_x, \hat{\omega}_x]$ (the roll angle might also be included but it can actually be dropped, owing to the rotational invariance of the problem).

(ii) For $m = \pm 1$ (helical modes), the force and torque are held by the vectors $y \mp \mathrm{i}z$ (up to complex conjugates). Projections of (2.13)–(2.15) along y and z can thus be combined so as to obtain a single equation for each of (2.13)–(2.15) in the plane of the disk. This is achieved by introducing the so-called $U(1)$ coordinates (Jenny & Dusek 2004) in the form $\hat{u}_\pm = \hat{u}_y \mp \mathrm{i}\hat{u}_z$, $\hat{\omega}_\pm = \hat{\omega}_z \pm \mathrm{i}\hat{\omega}_y$ and $\hat{\theta}_\pm = \hat{\theta}_z \pm \mathrm{i}\hat{\theta}_y$. The solid components associated with the eigenmodes for $m = \pm 1$ can thus be reduced to three complex numbers, namely $\hat{q}^b = [\hat{u}_m, \hat{\omega}_m, \theta_m]$.

(iii) For $|m| \geqslant 2$, the overall force and torque induced by the fluid component of the eigenmode vanish upon integration with respect to φ over $[0, 2\pi]$. Thus, there is no coupling between the fluid and body for these modes, so that the solid component $\hat{q}^b$ can simply be dropped from the problem, which becomes identical to that governing the stability of the flow past a fixed disk.

The problem (2.11)–(2.15) with appropriate boundary conditions can then be recast as a generalized eigenproblem in the form

$$\mathscr{A}_m \hat{q} = \lambda \mathscr{B}_m \hat{q}, \tag{2.17}$$

where

$$\mathscr{A}_m = \begin{pmatrix} \mathscr{A}^f_m(Re) & \mathscr{C} \\ \mathscr{F}_m(Re) & \mathscr{A}^b_m(Re, I^*) \end{pmatrix}, \quad \mathscr{B}_m = \begin{pmatrix} \mathscr{B}^f & 0 \\ 0 & \mathscr{B}^b_m(I^*) \end{pmatrix} \quad \text{and} \quad \hat{q} = \begin{pmatrix} \hat{q}^f \\ \hat{q}^b \end{pmatrix}. \tag{2.18}$$

The matrices $\mathscr{A}^f$ and $\mathscr{B}^f$ represent the linear operators acting only on the fluid variables $\hat{q}^f = [\hat{v}, \hat{p}]$. Similarly, $\mathscr{A}^b$ and $\mathscr{B}^b$ are the operators of the linearized rigid-body equations which only act on the disk kinematic variables $\hat{q}^b = [\hat{u}\pm, \hat{\omega}\pm, \hat{\theta}\pm]$. Terms $\mathscr{C}$ and $\mathscr{F}$ ensure the coupling between the body and fluid. The former expresses the action of the disk motion on the fluid flow (through the no-slip boundary condition on $\mathscr{S}$ and the presence of the body velocity and rotation rate in the Navier–Stokes equations), while the latter expresses to role of the fluid on the body motion through the hydrodynamic force and torque in (2.13) and (2.14), respectively. All submatrices are detailed in appendix B, as well as the symmetry conditions on the axis $\mathscr{S}_a$ to be retained for each value of m. As shown in appendix B, the case $m = 0$ yields only stable modes whose properties and spatial structure are discussed in appendix C. Since $|m| = 2$ modes do not influence the body path in the linear framework, we shall not discuss them any longer. Therefore, in the rest of the main text, we shall restrict the discussion to the case $|m| = 1$, or rather to $m = +1$ by taking advantage of the symmetries $(v_r, v_\varphi, v_x, p, u_x, u_+, \omega_+, \theta_+, m) \to (v_r, -v_\varphi, v_x, p, u_x, u_-, \omega_-, \theta_-, -m)$.

Note that modes with $m = +1$ and $\lambda_i > 0$ correspond to a right-handed helix, while those with $m = -1$ and $\lambda_i > 0$ correspond to a left-handed helix. In the framework of linear theory, both kinds of helices are admissible solutions, as well as any linear superposition of them. In particular, the superposition of right and left-handed helices of equal amplitudes yields a planar zigzagging path.

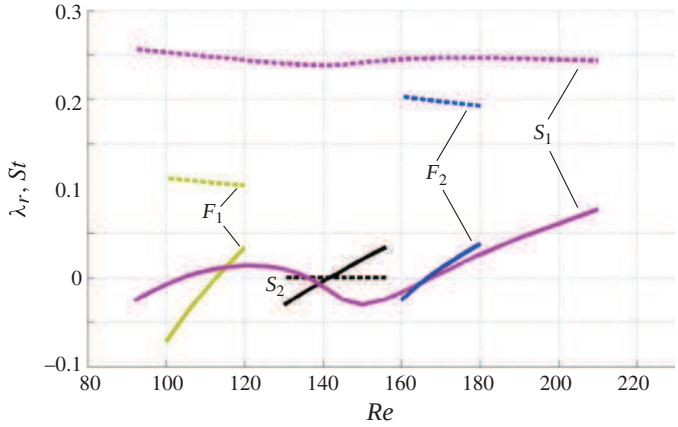

FIGURE 4. (Colour online) Critical eigenvalues for an infinitely thin disk at $I^* = 4 \times 10^{-3}$ and $Re \leqslant 220$. The growth rate (respectively frequency) of modes F_1, F_2, S_1 and S_2 is depicted with full (respectively dashed) lines. The plotted frequency is actually a Strouhal number defined as $St = \lambda_i/2\pi$.

3. The infinitely thin disk

3.1. *Parametric study*

We start discussing the results of the stability analysis by examining the limit case of an infinitely thin disk of finite inertia. Although unphysical strictly speaking, this limit is important to understand how very thin disks with a finite mass behave. In this case the definition of the dimensionless inertia I^* may be extended by introducing the surface density $\sigma_b = \lim_{\chi\to\infty} \rho_b h$, so that $I^* \to (\pi/64)\sigma_b/\rho d$. The disk we consider actually corresponds to $\chi = 10^4$ because the FreeFem++ solver requires the body to have a non-zero thickness. At such very large aspect ratios the precise value of χ has no influence, as shown by Meliga *et al.* (2009*a*) and Fabre *et al.* (2012) who employed the same software and recovered with disks corresponding to $\chi = 10^3$ and $\chi = 10^4$, respectively, the thresholds computed by Natarajan & Acrivos (1993) using a strictly infinitely thin disk.

The first important finding of the LSA is that at least four modes exist whatever I^*. One of them is stationary while the other three are oscillating. Hereinafter, these modes are identified as F_1, F_2, S_1 and S_2, with S referring to 'solid' and F to 'fluid' for reasons that will become evident later. Figure 4 illustrates the situation in the case of a disk with $I^* = 4 \times 10^{-3}$ by displaying the variations of the growth rate λ_r and Strouhal number $St = \lambda_i/2\pi$ with the Reynolds number. The S_2 mode is stationary ($\lambda_i = 0$) while F_1, F_2 and S_1 are oscillating (thus, corresponding to pairs of complex conjugates eigenvalues with $\lambda_i \neq 0$).

In the case of a disk held fixed in a uniform stream, the growth rate λ_r changes from negative to positive values at a critical Reynolds number Re_c and keeps positive values for larger Re. Figure 4 shows that more subtle scenarios can exist for a freely moving disk. Indeed the S_1 mode first becomes unstable for $Re \approx 104.4$, restabilizes at $Re \approx 136$ and destabilizes again at $Re \approx 167.7$. This 'destabilization–restabilization' process, which is not observed in some other ranges of I^*, was also noticed in the LSA of two-dimensional freely moving plates and rods (Assemat *et al.* 2012).

The four branches where a change of path occurs in a LSA perspective are gathered in figure 5. The grey-shaded area in that figure is the zone where a rectilinear vertical

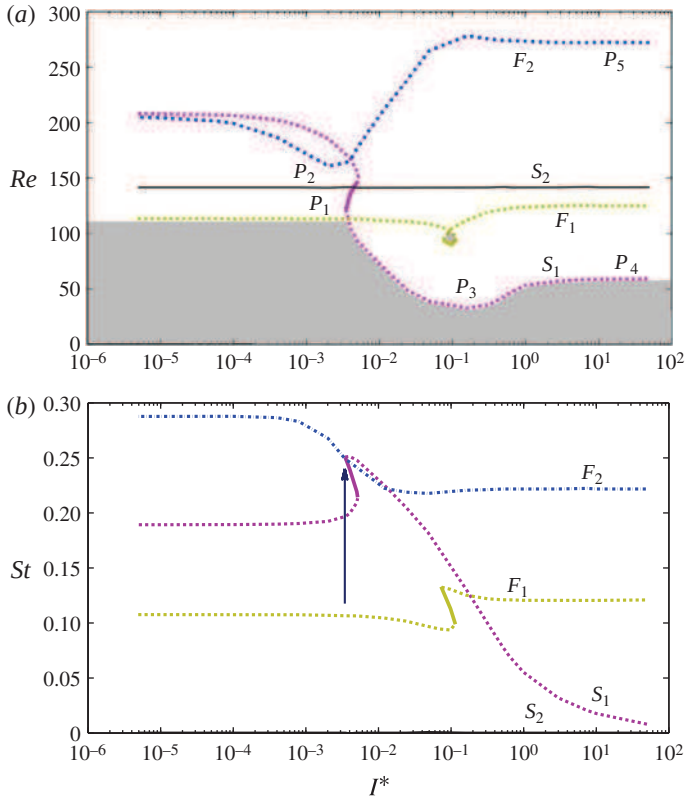

FIGURE 5. (Colour online) Neutral curves for an infinitely thin disk as a function of I^*: (*a*) Reynolds number; (*b*) Strouhal number. The solid part of the S_1 curve corresponds to the range where a destabilization–restabilization process takes place; the vertical arrow in (*b*) indicates the frequency jump associated with the switching from mode F_1 to mode S_1 along the critical curve.

path is stable with respect to infinitesimal disturbances. The curve corresponding to the S_1 branch shows that the destabilization–restabilization process mentioned earlier is actually confined within a narrow interval, typically $I^* \in [3.2 \times 10^{-3}, 5 \times 10^{-3}]$. The picture provided by figure 5 is exhaustive since all curves end with horizontal asymptotes corresponding to the limits $I^* \to \infty$ and $I^* \to 0$, respectively. The marginal curve corresponding to the minimum critical Reynolds number for each value of I^* is made of mode F_1 for $I^* \leqslant I^*_c \simeq 3.2 \times 10^{-3}$ and of mode S_1 for larger I^*. This mode switching has a spectacular consequence, as it is associated with a frequency jump from $St \approx 0.1$ to $St \approx 0.25$ as I^* crosses the critical value I^*_c; at large inertia ratios, the frequency of the S_1 mode is found to behave as $I^{*-1/2}$ (see figure 12*b*).

A surprising feature is the existence of a small stable subregion around $Re \approx 95$, $I^* \approx 0.09$. This subregion correspond to a 'loop' of the F_1 branch which turns back twice through two saddle nodes; accordingly, the lower part of the critical curve that joins those two points corresponds to a restabilization of the F_1 mode. This feature is qualitatively similar to the destabilization/restabilization event occurring along the S_1 branch, as illustrated in figure 4. According to figure 5(*b*), the frequency of the mode experiences a sharp variation in the range corresponding to this 'loop'.

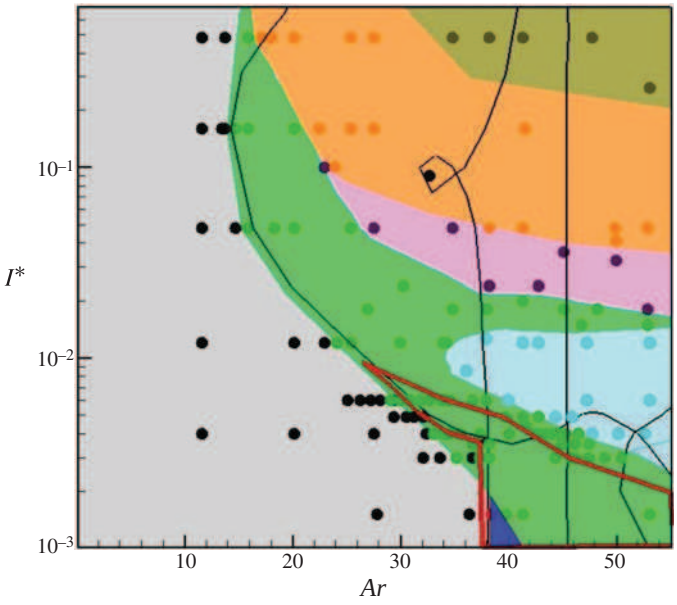

FIGURE 6. (Colour online) Comparison of thresholds provided by LSA (thin lines) with the regime map obtained through DNS by Auguste *et al.* (2013). Seven well-characterized regimes may be identified according to DNS data: the large area on the left (shown in grey) corresponds to the steady vertical fall; then increasing I^* along the right vertical axis of the figure one successively encounters a planar zigzagging (or fluttering) path (shown in green online) hereinafter termed as the *ZZ* regime, a helical zigzagging path termed 'hula-hoop' by Auguste *et al.* (shown in cyan online), a chaotic intermittent fluttering/tumbling regime (shown in purple online), a tumbling regime (shown in orange online) and a helical tumbling regime (shown in brown online). The thick curve (shown in red online) encloses the zone where small-amplitude '*A*-regimes' are observed; the small triangle at its bottom left corner (shown in blue online) corresponds to a small-amplitude zigzagging path (hereinafter termed as the ZZ_2 regime) with a frequency typically three times smaller than that of the main fluttering path.

Finally, LSA predicts that the stationary S_2 mode becomes unstable at $Re = 141.5$, i.e. $Ar \simeq 45.57$ (see figure 4), regardless of the disk inertia. This conclusion is in line with the weakly nonlinear predictions of Fabre *et al.* (2012) who determined that disks switch from a strictly vertical path to a *SO* path (which results from the addition of a stationary mode to the base flow) exactly for this value of Ar. That the S_2 branch is independent of I^* could have been inferred from the fact that inertia is not involved in (2.11)–(2.15) any more when $\lambda = 0$, as is the case at criticality with a stationary bifurcation.

3.2. *Comparison with available studies*

The complex behaviours displayed in figure 5 are far from being anecdotal. In particular, their comparison with the DNS data reported by Auguste *et al.* (2013) sheds light on a number of so far unexplained results. To evidence this, we made use of (2.10) to express the thresholds in terms of Ar rather than Re and switched the vertical and horizontal axes of figure 5(*a*) so as to obtain a direct comparison with the phase diagram displayed in figure 2 of Auguste *et al.* (2013). This procedure resulted in figure 6 which reveals that the marginal curve provided by the LSA matches the

I^*	Ar_c	St	(Stability branch)
1.5×10^{-3}	38.18	0.11	This study (F_1)
	38.0	0.11	DNS (Auguste *et al.* 2013) (thick line)
	38.31	0.11	DNS (Chrust *et al.* 2013)
4×10^{-3}	35.8	0.25	This study (S_1)
	33.0	0.29	DNS (Auguste *et al.* 2013) (left boundary of the fluttering regime)
	38.13	0.11	This study (F_1)
	34.3	0.1	DNS (Auguste *et al.* 2013) (thick line)
1.6×10^{-1}	14.3	0.13	This study (S_1)
	14.0	0.13	DNS (Auguste *et al.* 2013)
	22.87	0.14	QST (Fabre, Assemat & Magnaudet 2011)
5×10^{1}	22.77	0.0080	This study (S_1)
	22.87	0.0077	QST (Fabre *et al.* 2011)
I^*	Re_c	St	(Stability branch)
5×10^{1}	125.2	0.12	This study (F_1)
	125.3	0.12	LSA of the flow past a fixed disk (Meliga *et al.* 2009*b*)
5×10^{1}	272.25	0.22	This study (F_2)
	272.1	0.22	LSA of the flow past a fixed disk (unpublished)

TABLE 1. Comparison of thresholds and frequencies at representative values of I^*.

loss of the steady vertical path predicted by the DNS quite well, especially in the range $9 \times 10^{-3} \leqslant I^* \leqslant 3 \times 10^{-1}$. For lighter disks, the picture is complicated by the existence of small-amplitude regimes (called '*A*-regimes' by Ern *et al.* (2012)). The lower bound of the range of existence of the fluttering regime also departs from the neutral curve predicted by LSA, owing to the subcritical nature of the corresponding transition (Auguste *et al.* 2013; Chrust *et al.* 2013). Nevertheless, the thick line corresponding to the transition from steady vertical fall to the small-amplitude regimes is in perfect agreement with the prediction of LSA.

A noticeable discrepancy is also observed for $I^* > 3.5 \times 10^{-1}$: while DNS indicates that two successive transitions (vertical/fluttering and fluttering/tumbling) take place within the narrow range $15 \lesssim Ar \lesssim 17$, LSA still predicts a stable vertical path in that range. Here again, the subcritical nature of these transitions was numerically attested (Chrust *et al.* 2013).

Note that DNS confirms the existence of a stable vertical fall regime in a small region around $Ar \approx 36.0$ and $I^* \approx 0.09$, which coincides with the stable subregion embedded within the aforementioned 'loop' formed by the F_1 branch. In this range, the vertical path coexists with the large-amplitude tumbling motion but is only reached in DNS when using initial conditions very close to the vertical fall.

Apart from this peculiar feature, the higher branches predicted by the LSA do not seem to be relevant for determining the boundaries separating the various falling regimes. This is no surprise, owing to the linearity of this approach and the fact that it makes use of an axisymmetric base flow.

Table 1 displays, for some values of I^*, the values of Ar_c and St predicted by the present LSA and compares them with DNS data of Auguste *et al.* (2013) and

Chrust *et al.* (2013) and with predictions of the quasi-static theory (QST) developed by Fabre *et al.* (2011). A brief account of the assumptions underlying this theory and of its main results is provided in appendix D. Table 1 shows that the values of the Strouhal number St predicted by the LSA agree well with those reported in available DNS. In the small-I^* range, the two widely different frequencies reported in these studies and respectively associated with the ZZ and ZZ_2 regimes are faithfully recovered. Figure 5(*b*) reveals that these two frequencies are associated with two different unstable branches of the eigensolutions of (2.17), the ZZ mode being related to either F_2 or S_1 while the ZZ_2 mode is connected to F_1 (these modes are defined in the caption of figure 6). The situation is more complex for $I^* = 4 \times 10^{-3}$ where DNS predicts both a subcritical ZZ regime that sets in at $Ar = 33$ and is recovered by the LSA with a threshold located at $Ar = 35.8$, and a supercritical ZZ_2 regime that sets in at $Ar = 34.5$. The latter is not directly predicted by the LSA; however, the Strouhal number corresponding to this mode in the DNS is close to that characterizing the F_1 mode which becomes unstable at a somewhat larger value of Ar. We suspect that this regime results from nonlinear interactions between modes S_1 and F_1 as it occurs for a value of I^* very close to a point of codimension two corresponding to the intersection of the aforementioned two branches.

For moderate I^*, LSA predictions and DNS results match well regarding both the primary threshold Ar_c and the associated Strouhal number St. In contrast, the QST only captures properly the latter. This is in line with the findings of Assemat *et al.* (2012) who observed that QST correctly assesses the frequency down to moderate inertia ratios, whereas its predictions for the fluttering threshold are only reliable for large inertia ratios. That QST predictions for the fluttering threshold improve when I^* increases is obvious in table 1 (compare the predictions corresponding to $I^* = 1.6 \times 10^{-1}$ and $I^* = 5 \times 10^{1}$). Note that for $I^* = 1.6 \times 10^{-1}$, DNS predicts existence of a supercritical large-amplitude fluttering regime, thus closer to the ZZ type than to the ZZ_2 type despite a Strouhal number $\sim$0.13. As shown in figure 5(*b*), this is a range of I^* within which the S_1 and F_1 modes exhibit quite similar frequencies. This situation underlines the obvious fact that when several modes have quite similar frequencies, the mere knowledge of St provided by the LSA is not sufficient to predict the regime that is observed after nonlinear saturation. A weakly nonlinear analysis might help clarify this point. We shall see latter that useful information can also be obtained by examining the spatial structure of the unstable modes.

Results corresponding to $I^* = 5 \times 10^{1}$ show that the QST predictions compare well with those of the fully coupled LSA for large inertia ratios, thus validating the uncoupling of the body and fluid time scales on which QST is based (see appendix D). These results show that crossing the S_1 branch results in a slow ($St \approx 0.008$) unsteady motion of the disk with a quasi-steady wake. Finally table 1 shows that, for large I^*, the LSA recovers the existence of 'wake' (or 'fluid') modes. These are global modes which exist, with the same thresholds and frequencies, even if the disk is held fixed. Indeed, the first Hopf bifurcation for the flow past a fixed infinitely thin disk takes place at $Re_c \approx 125.3$ (Natarajan & Acrivos 1993; Meliga *et al.* 2009*b*) and oscillates at $St \approx 0.12$. Here this mode is found to be the asymptotic limit reached by the F_1 branch for large I^*. Also, we find that the asymptotic limit of the F_2 branch corresponds to a second oscillating mode. We performed a specific LSA of the flow past a fixed disk (with an independent stability code) and also detected this mode which sets in through a Hopf bifurcation at $Re_c \approx 272.1$ with $St \approx 0.22$, i.e. approximately a frequency twice that of the first 'fluid' mode. To the best of the authors' knowledge, this second Hopf mode has not been reported

previously. Its physical relevance is of course questionable, since the base flow is no longer axisymmetric at such values of Re. This mode may be seen as the counterpart for the disk of the second von Kármán mode predicted by LSA in the wake of two-dimensional fixed bodies (Assemat *et al.* 2012). That modes F_1 and F_2 may be identified with the two global modes observed past a fixed disk in the limit $I^* \to \infty$ justifies the terminology of 'fluid' modes, while modes S_1 and S_2 which are not found in the case of a fixed disk are clearly related to the degrees of freedom of the body and can then legitimately be referred to as 'solid' modes.

To summarize, comparison of LSA predictions with available DNS results reveals the relevance of the former approach which is found to properly recover the thresholds and frequency of most unstable modes detected in the DNS near the first unstable threshold. A noticeable gain with the LSA is the clear view it provides on the various unstable branches of the eigensolutions and on their asymptotic behaviours in the limit of small and large inertia ratios as well as on their possible crossings at specific values of I^*. The main issue we identified is the difficulty of a direct distinction between the ZZ and ZZ_2 regimes which strongly differ by their amplitude in the saturated state but may have similar frequencies in some range of I^*. We shall come back to this point later by examining the spatial structure of the oscillating modes.

3.3. *Global modes structure: segregation between fluid and body influences*

In the present section we seek to identify some key features of the spatial structure of the modes allowing us to assess, without performing full DNS computations, whether or not an unstable mode induces a strong or a weak coupling between the fluid and the body. For this purpose we select several points along the various branches of the stability diagram in the (I^*, Re) plane. Points P_1 to P_5 marked in figure 5 are chosen so as to gain some more insight into the nature of the observed disk motion and characteristics of the fluid–body coupling. Figure 7 displays the real (left) and the imaginary (right) parts of the global mode structure at each point P_i, normalized by the inclination angle $\theta_+ = \hat{\theta}_z \pm \mathrm{i}\hat{\theta}_y$. Given this definition of the inclination, the left column displays the modes in a state corresponding to the maximum of θ_z, whereas the right column corresponds to a state with $\theta_z = 0$ (and to a maximum θ_y in the case the path is three-dimensional). Note also that when $\theta_z = 0$, the z component of the rotation rate is maximum. The major advantage of this representation is that it provides a way to observe a given unsteady mode at two different instants of time; the case of a steady mode is slightly more subtle and will be detailed in § 4.

Both the real and the imaginary parts of the F_1 global mode at P_1 exhibit an alternation of positive and negative disturbances (emphasized by the streamline pattern) which is a clear footprint of wake oscillations. This wake structure very much resembles that behind a fixed disk (e.g. the 'fluid' mode at P_5 displayed in the last row), a feature worthy of interest since the point P_1 corresponds to a low value of I^*, i.e. to a situation where the disk is rather expected to be very sensitive to flow disturbances. Although surprising at first glance, this characteristics is in line with DNS observations where the first departure from the steady vertical fall in this range of I^* ($I^* \lesssim 3 \times 10^{-3}$) corresponds to the low-amplitude (or quasi-vertical) ZZ_2 regime (Auguste *et al.* 2013; Chrust *et al.* 2013), a regime that can hardly be properly characterized in experiments owing to residual disturbances in the fluid (Fernandes *et al.* 2007; Ern *et al.* 2012).

Although it corresponds to the same value of I^*, the F_2 mode at P_2 reveals an utterly different behaviour. This mode has a clear oscillating nature, as evidenced

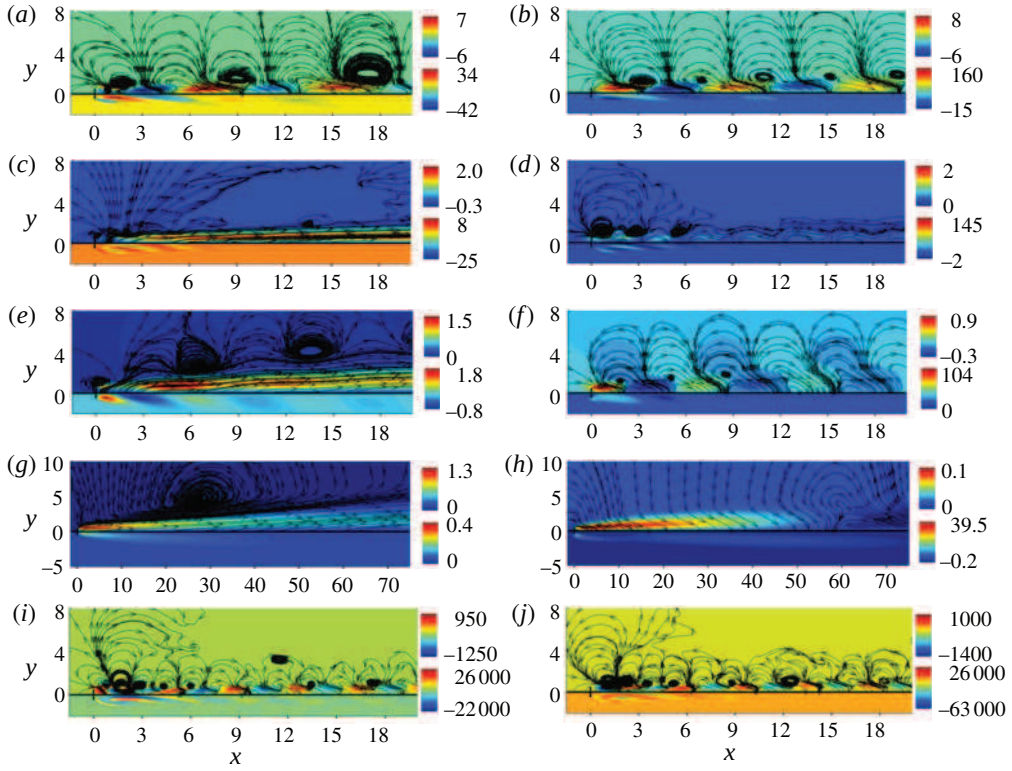

FIGURE 7. (Colour online) Global modes ($m = 1$) along the various branches of the stability diagram displayed in figure 5. Each row in the figure corresponds to a single point P_i, from $i=1$ at the top to $i=5$ at the bottom. The upper (respectively lower) half in each snapshot displays the axial velocity (respectively axial vorticity); streamlines are also drawn in the upper half. The left (respectively right) column show the real (respectively imaginary) part of the modes that have been normalized by the complex inclination θ_+. The five investigated points have the following (I^*, Re) coordinates: P_1 $(2 \times 10^{-3}, 113)$, P_2 $(2 \times 10^{-3}, 161.2)$, P_3 $(1.6 \times 10^{-1}, 33)$, P_4 $(50, 59.5)$, P_5 $(50, 273)$.

by the axial vorticity distribution in the near wake. However, the axial velocity distribution dramatically depends on which instant is chosen to observe it: while it takes the form of an elongated strip with a constant sign extending far downstream when $\theta_z = 1$, it reduces to a few rolls of alternating sign confined to the near wake when $\theta_z = 0$. Hence, unlike what we observed at P_1, a dramatic reorganization of the structure of the eigenmode within the wake takes place during the period of time separating the two snapshots. We interpret this reorganization as the footprint of the mutual coupling between the disk's degrees of freedom and its wake, a feature that appears to be much stronger on the F_2 mode at P_2 than in the previous case where the wake dynamics barely affect the motion of the disk. This corroborates the DNS results reported in figure 6. Indeed, for $I^* \simeq 1.5 \times 10^{-3}$, the DNS map predicts a transition from the A-regimes (enclosed within the thick line) to the large-amplitude ZZ fluttering regime for $Ar \simeq 55$, a value that compares well with the threshold value $Ar = 53$ predicted by the LSA at P_2 (the LSA prediction for the Strouhal number, $St \sim 0.29$, also agrees well with the DNS result).

The above interpretation of the differences revealed through the real and imaginary parts of the modes is also supported by what can be observed at point P_3. Given that the transition at P_3 is known from DNS to yield a supercritical large-amplitude ZZ regime despite a frequency ($St \simeq 0.13$) closer to that of mode F_1 at P_1 than to that of mode F_2 at P_2, we conclude that the similarities in the spatial structure of the associated global mode at points P_2 and P_3 allow us to anticipate that both of them are characterized by a strong fluid–body coupling. However, based on the qualitative degree of structural changes between the real and imaginary parts on the one hand and on the maximum of velocity and vorticity isovalues on the other hand, this coupling is likely to be stronger at P_2 than at P_3.

Therefore, our general statement is that all regimes in which the path of the disk exhibits large-amplitude horizontal deviations result from strong interactions between the body and its wake and share the linear signature unambiguously observed at point P_3. This common signature is such that the associated global mode successively exhibits disturbances of 'sign alternating type' (SAT) and of 'sign preserving type' (SPT). The former (figure 7*f*) involve rolls corresponding to clockwise and anticlockwise fluid motions which are intense only in the near wake, say up to $x \approx 3$, and then decrease downstream. In contrast the latter (figure 7*e*) take the form of an elongated strip of constant sign located along the wake axis, with only weak rolls aligned along the outer edge of this central region. The resemblance between the SPT wake structure and that of the wake behind a fixed disk just beyond the first bifurcation, which is known to yield non-zero stationary lift and torque, suggests that the effect of the SPT disturbances is to deviate the wake from its original orientation. When the disk moves freely, this deviation results in a drift between its geometrical axis and its translational velocity. Therefore a periodic motion of the disk can be understood from the succession of SAT and SPT disturbances, the former being responsible for fluid oscillations in the wake at each disk inclination, the latter modifying the disk inclination without much fluid oscillations.

The spatial structure of the global mode at P_4 on S_1 (figure 7*g–h*) is purposely represented over a very large domain downstream of the disk. This allows us to see the subtle switch from SPT to SAT structures that would be missed, had the mode structure been displayed over the same domain as in the previous figures. The snapshot in figure 7(*h*) shows that the wavelength of this SAT structure is very large. It then results in very slow oscillations, in agreement with the low frequency predicted by the QST. Moreover, the amplitude of the fluid velocity disturbance associated with this mode is weak, which suggests that it acts more on the disk than on the fluid. On the basis of the above criterion, this slow change from SPT to SAT structures implies that the coupling is very weak, although non-zero, the disk's influence manifesting itself only over a 'long' time scale. This is consistent with the separation of time scales at the root of the QST which qualifies this mode as 'aerodynamic' or 'solid', as opposed to the 'fluid' modes displayed in the snapshots in figure 7(*i,j*). In contrast with the previous case, both the real and imaginary parts of velocity and vorticity disturbances reach very large amplitudes in the wake at P_5. Therefore, the corresponding mode virtually acts only on the fluid, thus belonging to the 'fluid' category. The θ_z-independent behaviour of the SAT rolls revealed by these two snapshots confirms that there is almost no coupling between the disk and fluid motions for such large inertia ratios.

Finally, we may note that all of these results indicate that a strong fluid–body coupling is only observed with disks of low or moderate relative inertia, modes

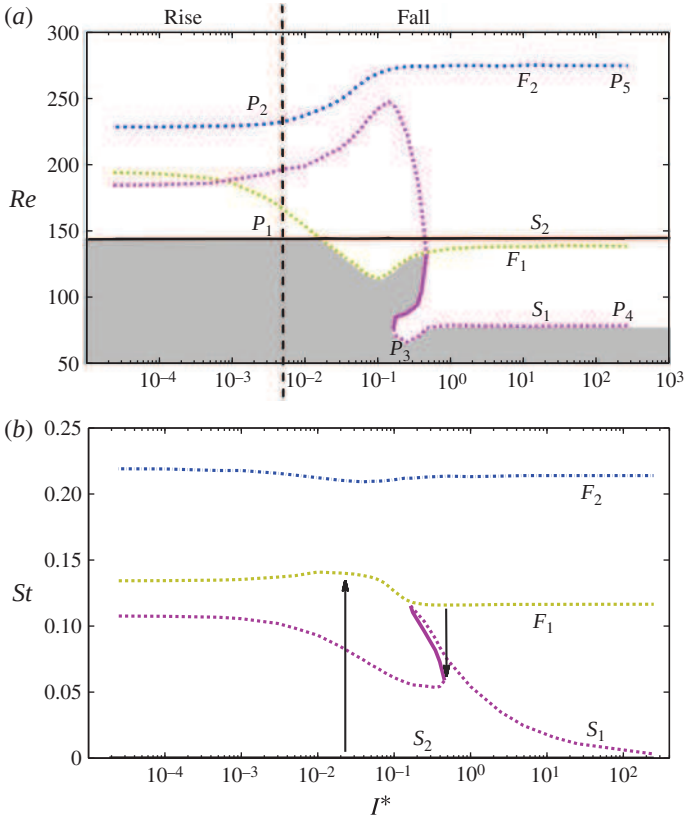

FIGURE 8. (Colour online) Neutral curves for a disk with $\chi = 10$. The same conventions are used as in figure 5. The dashed vertical line at $I^* = 4.908 \times 10^{-3}$ in (*a*) corresponds to disks with the same density as the fluid ($\bar{\rho} = 1$) and thus separates 'light' rising disks from 'heavy' falling disks.

P_2–P_3 belonging to the range of moderate I^* (say $I^* < 1.0$) while P_4 corresponds to a large value of I^*. The peculiar case of P_1 which belongs to the low-I^* range ($I^* = 2 \times 10^{-3}$) but displays a weak coupling behaviour underlines the complexity of the complete problem.

4. A thin disk with $\chi = 10$

We now consider the case of a disk of finite thickness such that $\chi = 10$. This specific geometry was employed in several previous experimental and computational studies, e.g. Fernandes *et al.* (2007) and Auguste *et al.* (2013) which focused on density ratios slightly lower than unity, i.e. on inertia ratios in the range $4 \times 10^{-3} \leqslant I^* \leqslant 5 \times 10^{-3}$. Selecting the same geometry will allow direct comparisons with these data and facilitate the interpretation of the stability branches.

Figure 8 gathers the four unstable branches of the eigensolutions of (2.17); the terminology used to identify them is similar to that of the previous section. Comparing the neutral curves of figure 8 with those of figure 5 reveals striking differences. Not only is the critical Reynolds number shifted towards higher values whatever I^* (see the general stability diagram in figure 12), but also the nature of the mode involved in the

first destabilization differs when I^* is small. This is noteworthy because experiments have long assumed that the disk aspect ratio does not play any role in the dynamics of the system, provided that it is 'sufficiently' large, which led to the building of regime maps gathering results obtained with disks of widely different aspect ratios, most of which in the range $10 \leqslant \chi \leqslant 10^2$ (Willmarth *et al.* 1964; Field *et al.* 1997). According to LSA predictions, the first bifurcation leading to a non-straight path for a thin disk with $\chi = 10$ is stationary for $I^* \leqslant 2 \times 10^{-2}$ (which corresponds to the S_2 branch in figure 8), leading to a *SO* path. This is in stark contrast with what we observed in figure 5 where the first bifurcation in this range of I^* is of Hopf type and thus leads to an oscillatory path. That the nature of the first non-vertical path of low-inertia disks crucially depends on their aspect ratio, even when it may be thought to be 'large', is in full agreement with the conclusions of Auguste *et al.* (2013) who provided a detailed comparison of the transition sequence for two disks with $\chi = \infty$ and $\chi = 10$, respectively, with $I^* \simeq 4 \times 10^{-3}$ in both cases. Indeed they found that the first non-vertical path of the latter is steady oblique while that of the former is time-dependent.

The crossing of modes S_2 and F_1 and of modes F_1 and S_1 along the critical marginal curve results in two frequency jumps (grey arrows in figure 8*b*). Again, a destabilization–restabilization subregion is found to exist on the S_1 branch in the range $1.6 \times 10^{-1} \leqslant I^* \leqslant 4.5 \times 10^{-1}$. For larger I^*, the stability diagram is qualitatively similar to that of an infinitely thin disk, with branches S_1, F_1, S_2 and F_2 successively crossed as Re increases. In the limit $I^* \to \infty$, the thresholds of branches F_1, F_2 and S_1 are found to be $Re \simeq 138.6$, $Re \simeq 274$ and $Re \simeq 78.6$, respectively. The independent LSA study we performed for the flow past a fixed disk with $\chi = 10$ confirmed the former two values (which justifies that modes associated with branches F_1 and F_2 be termed as 'fluid'), while the latter was recovered using the QST approach.

Let us now investigate the structural features of these modes at points P_i of the various branches of the stability diagram in figure 8(*a*). The axial velocity and vorticity of these modes are displayed in figure 9 using the same normalization as in figure 7. The first row corresponding to point P_1 shows that the structure of the associated primary mode requires a non-zero θ_z, since its imaginary part is uniformly null in our unit-inclination normalization. This global mode is thus tied to the tilt of the body and any disturbance in the fluid is merely a consequence of the disk being inclined. Since the SPT and SAT disturbances do not exist in this case, our previous criterion to assess the strength of the fluid–body coupling does not properly apply here, since there is no actual instant of time at which the body is uninclined. Nevertheless, it is clear that the stationary mode at P_1 corresponds to a one-way coupling, the wake being enslaved to the body.

The stationary mode consists of two time-independent counter-rotating vortices, leading to a permanent drift of the disk. This results in the so-called *SO* path whose occurrence and characteristics were predicted by Fabre *et al.* (2012) through a weakly nonlinear analysis. While the axial velocity strip well visible in figure 9(*a*) for $x \gtrsim 3$ results from the non-zero incidence angle of the disk, the existence of the standing eddy in the near wake ($x \lesssim 2$) helps explain how the zero-torque condition is satisfied along this steady path. Owing to the antisymmetry of modes $m = \pm 1$, the negative axial velocity disturbance seen in the upper half of figure 9(*a*) for $x \lesssim 2$ is positive in the lower half-plane, so that the negative velocities in the primary toroidal eddy are strengthened above the symmetry axis and weakened below it, yielding a larger drag on the disk in the upper half-plane and thus a positive torque tending to increase

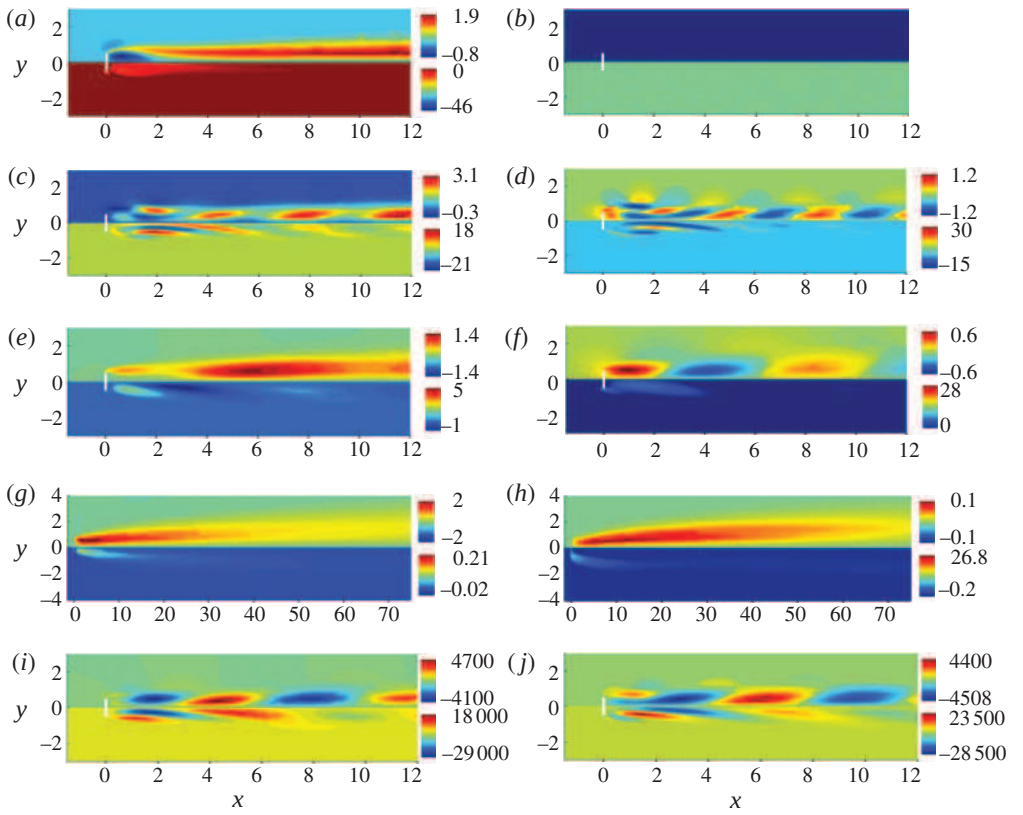

FIGURE 9. (Colour online) Global modes along the various branches of the stability diagram displayed in figure 8. Same convention as in figure 7. The five investigated points have the following (I^*, Re) coordinates: P_1 $(5 \times 10^{-3}, 144.2)$, P_2 $(5 \times 10^{-3}, 231.4)$, P_3 $(2.5 \times 10^{-1}, 65.4)$, P_4 $(25, 78.6)$, $P_5(25, 138.6)$.

the disk's inclination. This effect is balanced by the so-called 'restoring' added-mass torque which tends to realign the disk's velocity and symmetry axis, yielding an inclined path with a zero net torque.

Still for the same value of I^*, the structure of the global mode at P_2 shows that crossing the F_2 branch in this range of inertia ratios would lead to path oscillations caused by a rather strong mutual coupling between the body and fluid since the axial velocity disturbance switches from a SPT structure in the snapshot in figure 9(*c*) to a SAT structure in the snapshot in figure 9(*d*). This suggests rather large saturated amplitudes, in line with the DNS results which predict a *ZZ* flutter after a succession of *A*-regimes starting with the above steady oblique path. The correspondence with DNS predictions extends to the threshold and frequency: LSA predicts the F_2 mode to become unstable with $St = 0.22$ at $Re \simeq 231.4$ (corresponding to $Ar \simeq 66.8$), which compares fairly well with the DNS predictions $St = 0.205$, $Ar \simeq 63.5$ (Auguste *et al.* 2013) and experimental observations $St = 0.24$, $Ar = 70 \pm 3$ (Fernandes *et al.* 2007). The slightly lower threshold detected in the DNS is due to the subcritical nature of the corresponding bifurcation which was evidenced by Auguste *et al.* (2013) and Chrust *et al.* (2013).

The structures of the modes at P_3 and P_4 is displayed in the snapshots in figure 9(*e–h*). Both points belong to the S_1 branch along which St evolves as $I^{*-1/2}$ at large I^*. This low frequency is revealed by the large streamwise spacing between successive SAT disturbances in figure 9(*h,j*) which looks qualitatively similar to figure 7(*g,h*). The F_1 mode at P_5 (figure 9(*i,j*)) is qualitatively similar to its counterpart in figure 7: it is a pure fluid mode with virtually no influence on the disk motion (see the magnitude of the normalized velocity and vorticity disturbances), whose characteristics match those of the first oscillating mode past the disk held fixed. It is important to note that, although P_2 and P_5 both belong to the same F_2 branch, modes found along this branch deserve to be termed 'fluid' only in the large-I^* limit, since we found that the unstable mode at P_2 bears the mark of a significant mutual fluid–body coupling. Note that, on the basis of the differences in the geometry of the axial velocity and vorticity isocontours and in the corresponding isovalues, this coupling at P_2 is expected to be weaker than that at P_3, but stronger than that at P_4. This variation in the strength of the coupling with I^* in similar to that noticed in the case of an infinitely thin disk: the moderate-I^* range is that where the coupling appears to be the strongest, followed by the low-I^* range (say $I^* \leqslant 5 \times 10^{-3}$) and last by the range corresponding to large inertia ratios (say $I^* \geqslant 1.0$). This suggests that, in the same spirit as for the QST, a low-I^* theoretical model might be derived on the ground of a weak-coupling hypothesis.

5. A thick disk with $\chi = 3$

We finally consider a thick disk with an aspect ratio $\chi = 3$. This particular geometry has been used in several experimental and computational studies with an inertia ratio $I^* = 1.6 \times 10^{-2}$ corresponding to a body-to-fluid density ratio of 0.99. Although specific to this value of I^*, the corresponding findings provide a basis of comparison for the LSA results.

The stability diagram gathering the four neutral curves is displayed in figure 10. As with the previous two geometries, three of these curves are associated with a Hopf bifurcation while the fourth corresponds to a steady bifurcation. The critical curve is found to consist of the F_1 branch for $I^* \lesssim 0.28$, then the S_2 branch until $I^* \simeq 1$, and finally the S_1 branch for larger I^*. The frequency associated with this curve experiences two jumps encountered at those values of I^* corresponding to the two successive branch crossings. In contrast with the case of 'thin' disks, the stability diagram does no longer display any destabilization–restabilization region. In the whole range of inertia ratios, the S_1 branch is associated with low Strouhal numbers such that $St \leqslant 0.05$, while such a range was only encountered when $I^* > 1$ for 'thin' disks. Last but not least, in the limit $I^* \to \infty$, the thresholds corresponding to the three unsteady branches are exactly recovered by the QST which predicts $Re_c \simeq 114.7$ for the S_1 branch and $Re_c \simeq 177.5$ and $Re_c \simeq 300$ for the F_1 and F_2 branches, respectively.

The spatial structure of a few modes corresponding to points P_1 to P_3 in figure 10 is displayed in figure 11. The snapshots in figure 11(*a,b*) suggest that the Hopf bifurcation at P_1 on the F_1 branch involves a non-negligible but moderate coupling between the disk and its wake. This moderate coupling at low-I^* values is similar to what we observed with thin disks (compare with the snapshots in figure 9(*c,d*)).

Considerable changes are noticed between the two snapshots in figure 11(*c*) and (*d*) corresponding to point P_2 on the S_1 branch. Therefore, we expect this low-frequency mode ($St \simeq 0.039$) to involve a strong fluid–body coupling, certainly stronger than that at P_1. This contrasts with the behaviour of the thin disks considered so far, for which

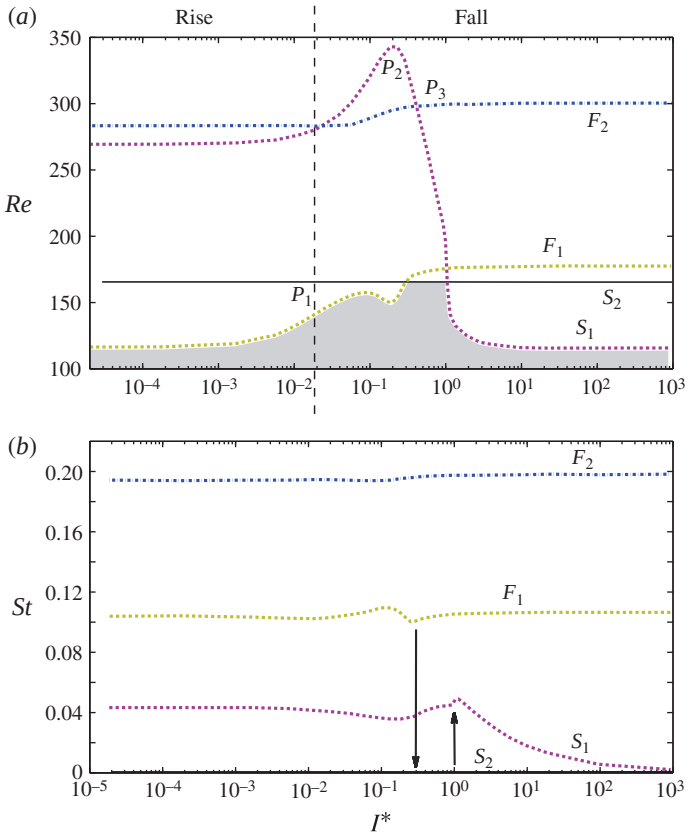

FIGURE 10. (Colour online) Neutral curves for a disk with $\chi = 3$. Same conventions as in figure 5.

a low-frequency regime was only encountered on the S_1 branch in the large-I^* range where the $St \propto I^{*-1/2}$ relation holds. In those cases, the unstable modes correspond to the quasi-static limit and hence induce only weak interactions between the body and its wake (e.g. figures 7*g*,*h* and 9*g*,*h*). What is qualitatively similar to the previous observations with thin disks and thus emerges as a general rule is that the strength of the fluid–body coupling reaches its maximum in the moderate-I^* range $5 \times 10^{-3} \leqslant I^* \leqslant 1.0$ to which P_2 belongs. That such a strong coupling, thus presumably leading to large-amplitude saturated oscillating motions with a Strouhal number as low as 0.04, may exist for a disk with $\chi = 3$ is not unlikely since planar *ZZ* regimes with Strouhal numbers in the range 0.025–0.045 have been observed with light falling spheres, both in DNS (Jenny *et al.* 2004) and in experiments (Veldhuis & Biesheuvel 2007). Hence, these low-frequency, yet with strong coupling, oscillating regimes seem to be specific to 'thick' bodies.

Finally, the snapshots in figure 11(*e*,*f*) display the unstable mode at P_3 along the F_2 branch. Although the large-I^* limit is not yet reached at this point, this mode behaves as if this were already the case: its structure being entirely made of SAT disturbances, it belongs to the 'fluid' type and barely affects the disk, as confirmed by the large values reached by the normalized vorticity disturbance.

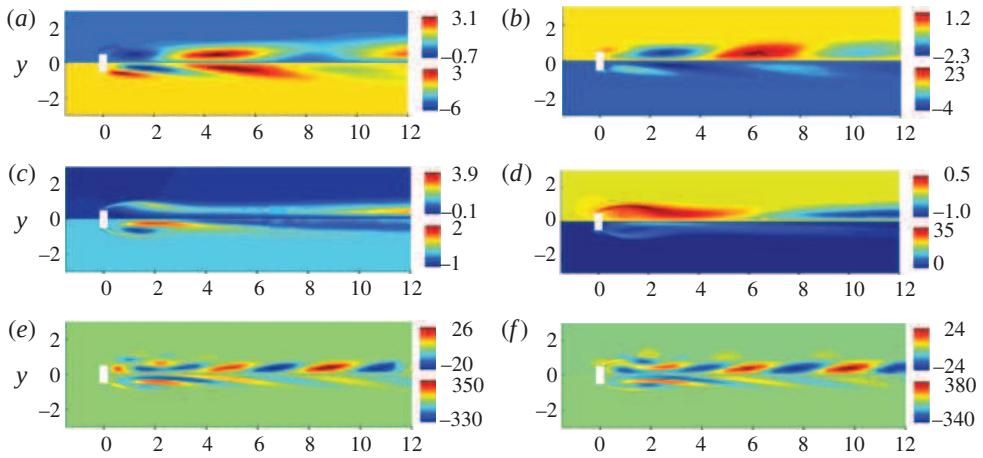

FIGURE 11. (Colour online) Global modes along the various stability branches of a thick disk with $\chi = 3$. The same conventions are used as in figure 7. The four investigated points have the following (I^*, Re) coordinates: P_1 $(1.9 \times 10^{-2}, 116.7)$, P_2 $(2.3 \times 10^{-1}, 342)$, P_3 $(5.6 \times 10^{-1}, 298)$.

6. Final discussion and conclusions

In this study, we have considered the path instability of a disk of arbitrary thickness rising or falling in a viscous fluid due to buoyancy/gravity in the framework of a global linear analysis. Three specific configurations corresponding to disks of aspect ratio $\chi = \infty$, 10 and 3 have successively been examined, the latter two been thought of as prototypes of thin and thick axisymmetric bodies, respectively. Using the axisymmetric flow past a disk moving broadside on as the base flow, we showed existence at any value of the inertia ratio I^* of four critical global modes with an azimuthal wavenumber $|m| = 1$. Three of them occur through a Hopf bifurcation while the fourth is associated with a stationary (pitchfork) bifurcation. The stability diagrams in the (I^*, Re) and (I^*, St) planes revealed rich and non-trivial behaviours, including several points corresponding to a codimension-two bifurcation, frequency jumps along the marginal curve and local regions where, for increasing Reynolds numbers, a restabilization can follow a destabilization.

The LSA results have frequently been compared with those of available DNS and experiments. We showed that they agree quantitatively well with previous findings regarding the primary destabilization, both on the thresholds and frequencies. Qualitatively, the spatial structure of the global modes normalized by the disk's inclination angle and visualized through its real and imaginary parts, made it possible to assess qualitatively the strength of the fluid–body coupling. We found that modes involving a moderate-to-strong (respectively weak) coupling generally induce large-(respectively small-)amplitude displacements of the disk in the saturated regime. Although this statement may appear quite strong at first glance, it was proved to be robust since our inferences based on LSA results match DNS predictions remarkably well. The transitions with a non-negligible mutual coupling were observed to have a common linear signature, namely a clear variation of the arrangement of axial velocity disturbances in the wake between the two different instants of time at which the corresponding mode is real or imaginary, respectively.

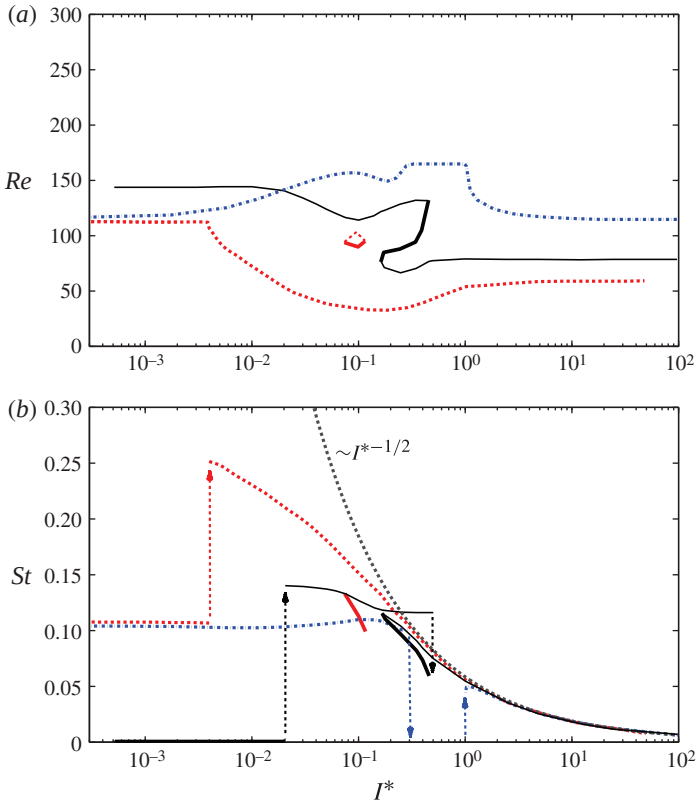

FIGURE 12. (Colour online) Superposition of: (*a*) the critical curves and (*b*) the corresponding frequencies for the three disks considered in this study: $\chi = \infty$ (dotted line, shown in red online), $\chi = 10$ (thin solid line, shown in black) and $\chi = 3$ (dash–dotted line, shown in blue online). The thick portions of the lines for $\chi = \infty$ and $\chi = 10$ indicate the restabilization branches; the arrows in (*b*) mark the frequency jumps.

In agreement with the recent weakly nonlinear analysis of Fabre *et al.* (2012), we found that the stationary mode predicted by the LSA in the freely moving disk problem, which exhibits an I^*-independent threshold, differs from its counterpart for a fixed disk, even in the large-I^* limit. It is worth noting that, still in the large-I^* limit, this mode is not the first to be destabilized whatever the disk aspect ratio. This contrasts with the fixed-body problem in which the wake always loses its axisymmetry through the stationary bifurcation. Again in the limit of large inertia ratios, LSA predicts existence of two unstable oscillating modes which are nothing but those associated with the linear wake instability past a fixed disk. These modes have been found to involve a negligible fluid–body coupling, the wake structure being independent of the disk's inclination, which led us to qualify them as 'fluid'. The general agreement between LSA predictions and DNS results proves unambiguously that the non-vertical regimes, be they *SO* or zigzag (either *ZZ* or ZZ_2), do not merely result from the dynamics of the sole wake but are intrinsic features resulting from the fully coupled fluid + disk problem, even though the coupling may in some cases be weak.

Finally, this study shed light on the crucial influence of the disk aspect ratio. This influence is summarized in figure 12 which gathers the critical curves and associated frequencies obtained for the three aspect ratios we considered. Figure 12(*a*) reveals that for $I^* \lesssim 2 \times 10^{-2}$, the thick disk with $\chi = 3$ deviates from a steady vertical path at a lower Reynolds number than the thin disk with $\chi = 10$, the infinitely thin disk being the most unstable of the three. In contrast, for larger inertia ratios, the primary instability threshold is a monotonically decreasing function of the aspect ratio, the system becoming unstable through a low-frequency mode in all cases. This decrease of Re_c as χ increases may be physically understood by noting that the larger χ the smaller the amount of fluid that must be displaced by the body to move edgewise. Hence, for given Re and I^* and a given disturbance in the disk's wake, one expects that the thicker the disk the less disturbed its motion. Thus, thick disks require larger wake disturbances, i.e. a larger Reynolds number, to start moving edgewise. Figure 12(*b*) shows that the oscillation frequency at the threshold is insensitive to the aspect ratio for $I^* \gtrsim 1$ since, in agreement with the scaling predicted by the QST, all curves collapse on the master curve $St \approx 5.8 \times 10^{-2} I^{*-1/2}$. According to (D 1), the existence of this master curve implies that, for a large enough relative inertia, the variation of the dimensionless torque experienced by the disk with respect to a change in its inclination (the coefficient $\mathscr{M}_{,\alpha}$ in (D 1)) does not depend on χ. The QST approximation also predicts that the threshold, Re_c, does not depend on I^*. However, as the comparison of the two subfigures shows, the latter prediction holds over a more narrow range of I^* than the former for the $St - I^*$ relation, a trend already noticed with two-dimensional plates (see figure 6 of Assemat *et al.* (2012)).

The transition scenario was found to be much more complex for low-inertia disks with two key features deserving further comments. One of these is that, although a disk with $\chi = 10$ may be thought of as thin, its behaviour still differs from that of an infinitely thin disk. In particular, the first unstable mode of the former in the low-I^* limit corresponds to a *SO* path while that of the latter results in a small-amplitude ZZ_2 fluttering motion. The other is that both of these modes induce bare lateral displacements of the disk, in contrast with the first unstable mode obtained for a thick disk with $\chi = 3$ which, still in the low-inertia limit, was observed to yield a *ZZ* regime corresponding to large-amplitude edgewise motions.

Differences between 'thin' and 'very thin' disks were already discussed by Auguste *et al.* (2013) and there is not much we can add here. From a physical point of view, the key reason we see for this influence of χ for already 'thin' disks is the 180° bending of the streamlines associated with flow disturbances around the edge: the thinner the body, the larger the local curvature of these streamlines. It would be of interest to determine beyond which aspect ratio the critical curve in figure 12 does not change significantly. We did not explore this question here. Nevertheless we may recall that the weakly nonlinear analysis of Fabre *et al.* (2012) showed that the stationary bifurcation from the base axisymmetric regime to the *SO* regime switches from supercritical to subcritical for $\chi \approx 52$. Hence, we expect the critical curve to remain of the same type as that corresponding to $\chi = 10$ in figure 12 for aspect ratios of several tens, until it eventually becomes qualitatively similar to that obtained with $\chi = \infty$.

Regarding contrasts in the magnitude of the body displacements for thin and thick disks in the low-inertia limit, we believe that it essentially finds its roots in the way the added-mass loads vary with χ. This may be appreciated by splitting the total hydrodynamic force and torque in (2.13)–(2.14) into added-mass contributions resulting from the non-penetration condition of the fluid at the body surface, and

vortical contributions keeping account of all viscous and wake effects (Howe 1995; Mougin & Magnaudet 2002*a*; Magnaudet 2011). Owing to the vanishing of the added-mass coefficient associated with edgewise translations in the limit $\chi \to \infty$, it may be shown that, for $I^* \to 0$, the in-plane projection of the force balance (2.13) indicates that the lateral component of the vortical force drives the inclination of the body but has no effect on its lateral drift (Fernandes *et al.* 2008), the latter being then entirely regulated by the torque balance through the so-called restoring added-mass torque. In contrast, when the two translational added-mass coefficients have a similar order of magnitude as is the case for $O(1)$ aspect ratios, the body primarily reacts to a lateral force disturbance through an edgewise acceleration, its inclination then being a direct consequence of the torque disturbance. Performing a perturbative analysis of (2.13)–(2.14) with $I^* = 0$ reveals that, for a given set of lateral force and torque disturbances, the lateral velocity of the body increases with its thickness. In other words, the decrease of the in-plane added-mass coefficient as $\chi \to \infty$ restricts the ability of thin bodies with negligible inertia to perform significant lateral oscillations, thus favouring the emergence of small-amplitude *A*-regimes.

Although inspection of the structure of the eigenmodes allows us, to a certain extent, to disentangle the 'fluid' and 'solid' contributions to the dynamics of the system in the vicinity of the primary thresholds, predicting the super/subcritical nature of the transitions and the amplitudes of the saturated states remain open questions which cannot be answered by linear theory. Thus, the next step beyond this work will be its extension to the weakly nonlinear regime, in the spirit of Meliga *et al.* (2009*a*) for fixed bodies and Fabre *et al.* (2012) for oblique steady paths. This extension should also allow us to consider modes interactions in the vicinity of the codimension-two points found at the crossings of primary branches for the three aspect ratios considered here. Such modes interactions are thought to be responsible for some complex features observed in DNS, especially for the existence of low-amplitude '*A*-regimes' for thin disks in some subranges of I^*.

Another limitation of the present approach is the choice of the broadwise vertical fall as the base state. Studying the stability properties of the edgewise fall could also provide interesting results, especially for thick disks. Indeed, both broadwise and edgewise motions were observed to be stable through DNS (Auguste 2010) for disks with $\chi = 1$. Both extensions will require performing the LSA in a fully three-dimensional framework, which is numerically quite challenging.

Acknowledgements

We are very grateful to P. Assemat for her help with the implementation of the FreeFem++ software for the coupled fluid–body eigenproblem. We also thank F. Auguste, who provided much of the DNS data used in the paper. This work was supported by the Agence Nationale de la Recherche under grant ANR-09-BLAN-0139 OBLIC.

Appendix A. Grid sensitivity

We already discussed the sensitivity of the computational approach used to solve the generalized eigenvalue problem to grid characteristics in previous papers (Assemat *et al.* 2012; Tchoufag *et al.* 2013). Here we present some additional tests performed to select the grid employed in the present study. Several grids were tested by varying successively the position of the inlet (L_1), outlet (L_2) and top (H) of the domain with respect to the body (see figure 2), as well as the number N_t of triangles involved in the discretization. Table 2 displays the variations of some quantities of interest

Grid	L_2	L_1	H	N_t	$C_D(Re=117)$	λ^{S_1}	λ^{F_1}	λ^{S_2}	λ^{F_2}
G1	76	23	33	20 693	1.197	$2.469\times10^{-3}\pm1.573i$	$6.264\times10^{-3}\pm0.667i$	3.395×10^{-3}	$4.580\times10^{-3}\pm1.248i$
G2	101	23	33	22 091	1.196	$2.804\times10^{-3}\pm1.571i$	$6.373\times10^{-3}\pm0.667i$	3.417×10^{-3}	$5.030\times10^{-3}\pm1.248i$
G3	76	44	33	21 963	1.196	$2.618\times10^{-3}\pm1.572i$	$6.259\times10^{-3}\pm0.667i$	3.410×10^{-3}	$4.862\times10^{-3}\pm1.248i$
G4	76	23	55	23 849	1.197	$2.216\times10^{-3}\pm1.572i$	$6.252\times10^{-3}\pm0.667i$	3.346×10^{-3}	$4.746\times10^{-3}\pm1.248i$
G5	76	23	33	29 970	1.197	$2.221\times10^{-3}\pm1.572i$	$6.330\times10^{-3}\pm0.667i$	3.526×10^{-3}	$4.846\times10^{-4}\pm1.248i$

TABLE 2. Influence of grid characteristics on some selected quantities of interest. The values of the critical Reynolds number for modes S_1, F_1, S_2 and F_2 are $Re\simeq106$, 114, 143 and 168, respectively.

when considering the instability past an infinitely thin disk with $I^* = 4 \times 10^{-2}$; the corresponding growth rates and frequencies are displayed in figure 4. The drag coefficient C_D in the base flow right at the threshold of the first instability, $Re_c = 117$ (corresponding to figure 3), and the imaginary part of the three complex eigenvalues S_1, F_1 and F_2 slightly above the corresponding threshold are found to be almost insensitive to the variations of grid parameters in the range explored in table 2. The growth rate reveals some variations, especially regarding modes S_1 and F_2. We combined these results with a similar determination of the (negative) growth rates just below the thresholds. Based on these various results, we concluded that grids 2 and 3 are slightly less accurate than the other three and we finally selected grid 1 as the best compromise between accuracy and computational time. All results discussed in the paper were obtained with that grid.

Appendix B. The generalized eigenproblem for the coupled fluid–body system

The set of linear equations to be solved is given by (2.11)–(2.15). Seeking solutions in the form of normal modes (2.16) and defining I^{**} as $I^*/(1 + (4/3)\chi^{-2})$ yields

$$\begin{aligned}
\lambda\hat{v} &= -(V_0 - U_0)\cdot\nabla_m\hat{v} - (\hat{v} - (\hat{u} + \hat{\omega}\times r)\mathrm{e}^{-\mathrm{i}m\varphi})\cdot\nabla V_{\mathbf{0}} - \hat{\omega}\mathrm{e}^{-\mathrm{i}m\varphi}\times V_{\mathbf{0}} \\
&\quad - \nabla_m\hat{p} + Re^{-1}\nabla_m^2\hat{v}, && \text{(B 1)}\\
0 &= \nabla_m\cdot\hat{v}, && \text{(B 2)}\\
16\lambda I^{**}\hat{u} &= -16I^{**}\hat{\omega}\times U_0 + D_0(\hat{\theta}_z y - \hat{\theta}_y z) \\
&\quad + \int_{\mathscr{S}} [\hat{f}_x x + (\hat{f}_r\cos\varphi - \hat{f}_\varphi\sin\varphi)y + (\hat{f}_r\sin\varphi + \hat{f}_\varphi\cos\varphi)z]\mathrm{e}^{\mathrm{i}m\varphi}\,\mathrm{d}S, && \text{(B 3)}\\
\lambda\mathbb{I}^*\cdot\hat{\omega} &= \int_{\mathscr{S}} [r\hat{f}_\varphi x + \left((r\hat{f}_x - x\hat{f}_r)\sin\varphi - x\hat{f}_\varphi\cos\varphi\right) y \\
&\quad + ((x\hat{f}_r - r\hat{f}_x)\cos\varphi - x\hat{f}_\varphi\sin\varphi)z]\mathrm{e}^{\mathrm{i}m\varphi}\,\mathrm{d}S, && \text{(B 4)}\\
\lambda\hat{\xi} &= \hat{\omega}. && \text{(B 5)}
\end{aligned}$$

where $\nabla_m = (\partial_r, \mathrm{i}m/r, \partial_x)$ and $(\hat{f}_r, \hat{f}_\varphi, \hat{f}_x)^{\mathrm{T}} = \hat{t}_m\cdot n$, $\hat{t}_m = -\hat{p}I + Re^{-1}(\nabla_m\hat{v} + (\nabla_m\hat{v})^{\mathrm{T}})$ being the disturbance stress tensor relative to mode m.

The boundary conditions to be satisfied by the fluid components of the problem on the symmetry axis $\mathscr{S}_a$ depend on the value of the azimuthal wavenumber. After some inspection one finds:

(i) for $m = 0$: $\hat{v}_r = \partial_r\hat{v}_x = \partial_r\hat{p} = 0$;
(ii) for $|m| = 1$: $\partial_r\hat{v}_r = \partial_r\hat{v}_\varphi = \hat{v}_x = \hat{p} = 0$.

Finally, projecting (B 3)–(B 5) onto each axis of the moving frame of reference (x, y, z) yields different sets of rigid-body motion equations, depending on the value of m under consideration. These equations are detailed in the following subsections.

B.1. *Case* $m = 0$

Since this mode preserves axial symmetry (possibly with swirl), only $\hat{u}_x$ and $\hat{\omega}_x$ can be non-zero provided $\lambda \neq 0$. Noting that n_x is non-zero (actually $n_x = \pm 1$) only on the front and back faces of the disk where $\mathrm{d}S = r\,\mathrm{d}r\,\mathrm{d}\varphi$, while n_r is non-zero (actually $n_r = 1$) only on its lateral surface where $\mathrm{d}S = \mathrm{d}x\,\mathrm{d}\varphi/2$, the eigenproblem reduces to

$$8I^{**}\lambda\hat{u}_x = \pi\int_{\mathscr{S}}\left[(-\hat{p} + 2Re^{-1}\partial_x\hat{v}_x)n_x r\,\mathrm{d}r + \frac{1}{2}Re^{-1}(\partial_r\hat{v}_x + \partial_x\hat{v}_r)n_r\,\mathrm{d}x\right], \qquad \text{(B 6)}$$

$$\lambda I^{**}\hat{\omega}_x \;=\; \pi Re^{-1}\int_{\mathscr{S}}\left[(\partial_x\hat{v}_\varphi)n_x r^2\,\mathrm{d}r+\frac{1}{2}\left(\partial_r\hat{v}_\theta-\frac{\hat{v}_\varphi}{r}\right)n_r\,\mathrm{d}x\right]. \tag{B 7}$$

This problem may be recast in the generic form

$$\lambda\mathscr{B}_0\hat{q}_0=\mathscr{A}_0\hat{q}_0 \tag{B 8}$$

by defining

$$\mathscr{A}_0=\begin{pmatrix}-\mathscr{C}_0(\cdot,\,V_0)+Re^{-1}\nabla_0^2(\cdot) & -\nabla_0(\cdot) & \partial_x\,(V_{0r}e_r+V_{0x}x) & -V_{0r}e_\varphi\\ \nabla_0\cdot(\cdot) & 0 & 0 & 0\\ \mathscr{F}^v(\cdot) & \mathscr{F}^p(\cdot) & 0 & 0\\ \mathscr{M}^v(\cdot) & 0 & 0 & 0\end{pmatrix}, \tag{B 9}$$

$$\mathscr{B}_0=\begin{pmatrix}I & 0 & 0 & 0\\ 0 & 0 & 0 & 0\\ 0 & 0 & 8I^{**} & 0\\ 0 & 0 & 0 & I^{**}\end{pmatrix}\quad\text{and}\quad \hat{q}_0=\begin{pmatrix}\hat{v}\\ \hat{p}\\ \hat{u}_x\\ \hat{\omega}_x\end{pmatrix}, \tag{B 10}$$

with $\mathscr{C}_m(\hat{v},\,V_0)=(V_0-U_0)\cdot\nabla_m\hat{v}+\hat{v}\cdot\boldsymbol{\nabla}V_0$, $\mathscr{F}^v$ (respectively $\mathscr{M}^v$) and $\mathscr{F}^p$ being the operators that generate the viscous and pressure contributions to the hydrodynamic force (respectively torque). Here $\mathscr{F}^v(\hat{v}_0)$ and $\mathscr{F}^p(\hat{p}_0)$ correspond to the right-hand side of (B 6), while $\mathscr{M}^v(\hat{v}_0)$ corresponds to that of (B 7). In the eigenproblem (B 8), the boundary conditions are imposed through a penalization method. For instance, the no-slip condition on the disk surface is satisfied by inserting the equation $\varepsilon_p{}^{-1}[\hat{v}-\hat{u}_x x-r\hat{\omega}_x e_\varphi]=\mathbf{0}$ with $\varepsilon_p\ll 1$ in the rows of the matrices $\mathscr{A}_0$ and $\mathscr{B}_0$ corresponding to boundary nodes, i.e. by replacing the first row of $\mathscr{A}_0$ (respectively $\mathscr{B}_0$) with $(\varepsilon_p^{-1},\,0,\,-\varepsilon_p^{-1}x,\,-\varepsilon_p^{-1}re_\varphi)$ (respectively 0). In this way, the boundary condition is satisfied if ε_p is selected small enough for $O(\varepsilon_p^{-1})$ terms to dominate all other terms at these nodes.

B.2. *Case* $m=\pm1$

In this mode, $\hat{u}_x=\hat{\omega}_x=0$ provided that $\lambda\neq0$, so that

$$\begin{aligned}16\lambda I^{**}\hat{u}_y=\;&16I^{**}U_0\hat{\omega}_z+D_0\hat{\theta}_z\\ &+\pi\int_{\mathscr{S}}\left[\frac{1}{2}(-\hat{p}+2Re^{-1}\partial_r\hat{v}_r)n_r\,\mathrm{d}x+Re^{-1}(\partial_r\hat{v}_x+\partial_x\hat{v}_r)n_x r\,\mathrm{d}r\right]\\ &\mp\mathrm{i}\pi Re^{-1}\int_{\mathscr{S}}\left[\frac{1}{2}\left(\partial_r\hat{v}_\varphi-\frac{\hat{v}_\varphi}{r}\pm\frac{\mathrm{i}}{r}\hat{v}_r\right)n_r\,\mathrm{d}x\right.\\ &\left.+\left(\partial_x\hat{v}_\varphi\pm\frac{\mathrm{i}}{r}\hat{v}_x\right)n_x r\,\mathrm{d}r\right],\end{aligned} \tag{B 11}$$

$$\begin{aligned}16\lambda I^{**}\hat{u}_z=\;&-16I^{**}U_0\hat{\omega}_y-D_0\hat{\theta}_y\\ &\pm\mathrm{i}\pi\int_{\mathscr{S}}\left[\frac{1}{2}(-\hat{p}+2Re^{-1}\partial_r\hat{v}_r)n_r\,\mathrm{d}x+Re^{-1}(\partial_r\hat{v}_x+\partial_x\hat{v}_r)n_x r\,\mathrm{d}r\right]\\ &+\pi Re^{-1}\int_{\mathscr{S}}\left[\frac{1}{2}\left(\partial_r\hat{v}_\varphi-\frac{\hat{v}_\varphi}{r}\pm\frac{\mathrm{i}}{r}\hat{v}_r+\right)n_r\,\mathrm{d}x+\left(\partial_x\hat{v}_\varphi\pm\frac{\mathrm{i}}{r}\hat{v}_x\right)n_x r\,\mathrm{d}r\right],\end{aligned} \tag{B 12}$$

$$\lambda I^*\hat{\omega}_y = \pm \mathrm{i}\pi \int_{\mathscr{S}} r\left[(-\hat{p}+2Re^{-1}\partial_x\hat{v}_x)n_x r\,\mathrm{d}r + \frac{1}{2}Re^{-1}(\partial_r\hat{v}_x+\partial_x\hat{v}_r)n_r\,\mathrm{d}x\right]$$
$$\mp \mathrm{i}\pi \int_{\mathscr{S}} x\left[\frac{1}{2}(-\hat{p}+2Re^{-1}\partial_r\hat{v}_r)n_r\,\mathrm{d}x + Re^{-1}(\partial_r\hat{v}_x+\partial_x\hat{v}_r)n_x r\,\mathrm{d}r\right]$$
$$-\pi\int_{\mathscr{S}} x\left[\frac{1}{2}Re^{-1}\left(\partial_r\hat{v}_\varphi - \frac{\hat{v}_\varphi}{r} \pm \frac{\mathrm{i}}{r}\hat{v}_r\right)n_r\,\mathrm{d}x\right.$$
$$\left. + Re^{-1}\left(\partial_x\hat{v}_\varphi \pm \frac{\mathrm{i}}{r}\hat{v}_x\right)n_x r\,\mathrm{d}r\right], \tag{B 13}$$

$$\lambda I^*\hat{\omega}_z = -\pi\int_{\mathscr{S}} r\left[(-\hat{p}+2Re^{-1}\partial_x\hat{v}_x)n_x r\,\mathrm{d}r + \frac{1}{2}Re^{-1}(\partial_r\hat{v}_x+\partial_x\hat{v}_r)n_r\,\mathrm{d}x\right]$$
$$+\pi\int_{\mathscr{S}} x\left[\frac{1}{2}(-\hat{p}+2Re^{-1}\partial_r\hat{v}_r)n_r\,\mathrm{d}x + Re^{-1}(\partial_r\hat{v}_x+\partial_x\hat{v}_r)n_x r\,\mathrm{d}r\right]$$
$$\mp \mathrm{i}\pi\int_{\mathscr{S}} x\left[\frac{1}{2}Re^{-1}\left(\pm\frac{\mathrm{i}}{r}\hat{v}_r + \partial_r\hat{v}_\varphi - \frac{\hat{v}_\varphi}{r}\right)n_r\,\mathrm{d}x\right.$$
$$\left. + Re^{-1}\left(\partial_x\hat{v}_\varphi \pm \frac{\mathrm{i}}{r}\hat{v}_x\right)n_x r\,\mathrm{d}r\right], \tag{B 14}$$

$$\lambda\hat{\theta}_y = \hat{\omega}_y, \tag{B 15}$$

$$\lambda\hat{\theta}_z = \hat{\omega}_z. \tag{B 16}$$

Using the $U(1)$-coordinate transformation $\hat{u}_\pm = \hat{u}_y \mp \mathrm{i}\hat{u}_z$, $\hat{\theta}_\pm = \hat{\theta}_z \pm \mathrm{i}\hat{\theta}_y$ and $\hat{\omega}_\pm = \hat{\omega}_z \pm \mathrm{i}\hat{\omega}_y$, the y and $\mathrm{i}z$ projections can be added so as to reduce the body equations for helical disturbances to

$$16\lambda I^{**}\hat{u}_\pm = \pm 16\mathrm{i}I^{**}U_0\hat{\omega}_\pm \pm \mathrm{i}D_0\hat{\theta}_\pm$$
$$+2\pi\int_{\mathscr{S}}\left[\frac{1}{2}(-\hat{p}+2Re^{-1}\partial_r\hat{v}_r)n_r\,\mathrm{d}x + Re^{-1}(\partial_r\hat{v}_x+\partial_x\hat{v}_r)n_x r\,\mathrm{d}r\right]$$
$$\mp 2\mathrm{i}\pi Re^{-1}\int_{\mathscr{S}}\left[\frac{1}{2}\left(\partial_r\hat{v}_\varphi - \frac{\hat{v}_\varphi}{r}\pm\frac{\mathrm{i}}{r}\hat{v}_r\right)n_r\,\mathrm{d}x + \left(\partial_x\hat{v}_\varphi\pm\frac{\mathrm{i}}{r}\hat{v}_x\right)n_x r\,\mathrm{d}r\right], \tag{B 17}$$

$$\lambda I^*\hat{\omega}_\pm = \mp 2\pi\int_{\mathscr{S}} r\left[(-\hat{p}+2Re^{-1}\partial_x\hat{v}_x)n_x r\,\mathrm{d}r + \frac{1}{2}Re^{-1}(\partial_r\hat{v}_x+\partial_x\hat{v}_r)n_r\,\mathrm{d}x\right]$$
$$\pm 2\pi\int_{\mathscr{S}} x\left[\frac{1}{2}(-\hat{p}+2Re^{-1}\partial_r\hat{v}_r)n_r\,\mathrm{d}x + Re^{-1}(\partial_r\hat{v}_x+\partial_x\hat{v}_r)n_x r\,\mathrm{d}r\right]$$
$$-2\pi\int_{\mathscr{S}} x\left[\frac{1}{2}Re^{-1}\left(\partial_r\mathrm{i}\hat{v}_\varphi - \frac{\mathrm{i}\hat{v}_\varphi}{r}\mp\frac{\hat{v}_r}{r}\right)n_r\,\mathrm{d}x\right.$$
$$\left. + Re^{-1}\left(\partial_x\mathrm{i}\hat{v}_\varphi\mp\frac{\hat{v}_x}{r}\right)n_x r\,\mathrm{d}r\right], \tag{B 18}$$

$$\lambda\hat{\theta}_\pm = \hat{\omega}_\pm. \tag{B 19}$$

Comparing (B 18) with (B 13)–(B 14) shows that $\hat{\omega}_\pm = 2\hat{\omega}_z = \pm 2\mathrm{i}\hat{\omega}_y$, so that (B 19) and (B 15)–(B 16) imply $\hat{\theta}_\pm = 2\hat{\theta}_z = \pm 2\mathrm{i}\hat{\theta}_y$. Introducing these results into (B 11)–(B 12) and comparing with (B 17) finally shows that $\hat{u}_\pm = 2\hat{u}_y = \pm 2\mathrm{i}\hat{u}_z$. This could have

been inferred from the fact that the transformation $(\hat{u}_y,\ \hat{\omega}_z,\ \hat{\theta}_z) \rightarrow \pm\mathrm{i}(\hat{u}_z,\ \hat{\omega}_y,\ \hat{\theta}_y)$ for $m = \pm 1$ interchanges the y and z projections. Taking the above relations into consideration and introducing the $U(1)$-coordinate transformation in the fluid equations, the eigenproblem may finally be written in the form

$$\lambda \mathscr{B}_{\pm 1}\hat{q}_{\pm 1} = \mathscr{A}_{\pm 1}\hat{q}_{\pm 1} \tag{B 20}$$

with

$$\mathscr{A}_{\pm 1} = \begin{pmatrix} -\mathscr{C}_1(\cdot, V_0) + Re^{-1}\nabla_1^2(\cdot) & -\nabla_1(\cdot) & \frac{1}{2}\partial_r\left(V_{0r}e_r + V_{0x}x\right) & \mp\frac{1}{2}\left[r\partial_x\left(V_{0r}e_r + V_{0x}x\right) - \left(V_{0x}e_r + V_{0r}e_x\right)\right] & 0 \\ & & \pm\frac{1}{2}\mathrm{i}\frac{V_{0r}}{r}e_\varphi & \pm\frac{1}{2}x\partial_r\left(V_{0r}e_r + V_{0x}x\right) + \frac{1}{2}\mathrm{i}\left[x\frac{V_{0r}}{r} - V_{0x}\right]e_\varphi & 0 \\ \nabla_1\cdot(\cdot) & 0 & 0 & 0 & 0 \\ \mathscr{F}^v(\cdot) & \mathscr{F}^p(\cdot) & 0 & 16I^{**}U_0 & D_0 \\ \mathscr{M}^v(\cdot) & \mathscr{M}^p(\cdot) & 0 & 0 & 0 \\ 0 & 0 & 0 & 1 & 0 \end{pmatrix}, \tag{B 21}$$

$$\mathscr{B}_{\pm 1} = \begin{pmatrix} I & 0 & 0 & 0 & 0 \\ 0 & 0 & 0 & 0 & 0 \\ 0 & 0 & 16I^{**} & 0 & 0 \\ 0 & 0 & 0 & I^* & 0 \\ 0 & 0 & 0 & 0 & 1 \end{pmatrix} \quad \text{and} \quad \hat{q}_{\pm 1} = \begin{pmatrix} \hat{v} \\ \hat{p} \\ \hat{u}_\pm \\ \hat{\omega}_\pm \\ \hat{\theta}_\pm \end{pmatrix}, \tag{B 22}$$

where $\mathscr{F}^v(\hat{v}_1)$ and $\mathscr{F}^p(\hat{p}_1)$ (respectively $\mathscr{M}^v(\hat{v}_1)$ and $\mathscr{M}^p(\hat{p}_1)$) correspond to the right-hand side of (B 17) (respectively (B 18)).

Appendix C. The $m = 0$ modes

In this appendix we comment on the thresholds and spatial structures of the $m = 0$ mode. Although this family of modes cannot lead to path instability for reasons discussed in § 2, it may be of importance in future weakly nonlinear studies. To illustrate the behaviour and structure of the $m = 0$ modes, we solve (B 8) in the case of an infinitely thin disk. We select two values of the inertia ratio corresponding to points P_1 ($I^* = 5 \times 10^{-3}$) and P_5 ($I^* = 5 \times 10^{1}$) in figure 5. Three axisymmetric global modes are observed. They are all found to be stationary ($St = 0$) and stable as illustrated by their negative growth rates displayed in figure 13, even though two of them are almost neutral in the limit $I^* \rightarrow \infty$ (see the inset in figure 13).

From the structure of (B 7), (B 9) and (B 10), one can separate the axisymmetric modes into two families: U_{RX} and U_P. The first (respectively second) family is made of modes whose velocity components lie along $\hat{e}_r$ and $\hat{e}_x$ (respectively $\hat{e}_\varphi$) and thus yield a purely azimuthal (respectively axial and radial) vorticity field. On this basis we find that, whatever the inertia ratio, two series of modes belong to U_{RX} and only one belongs to U_P. Their structure at $Re = 328$ is displayed in figure 14 where, for obvious reasons, U_{RX} (respectively U_P) modes have been normalized by $\hat{u}_x$ (respectively $\hat{\omega}_x$).

The large isovalues of the axial velocity and azimuthal vorticity observed for the U_{RX} mode displayed in the snapshot in figure 14(f) indicate that the corresponding mode has a 'fluid' nature, i.e. it could also have been obtained by studying the wake of a fixed disk (this is why the corresponding curve is labelled 'F' in figure 13). In contrast the two almost neutral modes displayed in the snapshots in figure 14(b,d) are tied to the body degrees of freedom and could also be retrieved by using the QST summarized in appendix D. Their small growth rates result from the $|\lambda_r| \sim I^{*-1}$

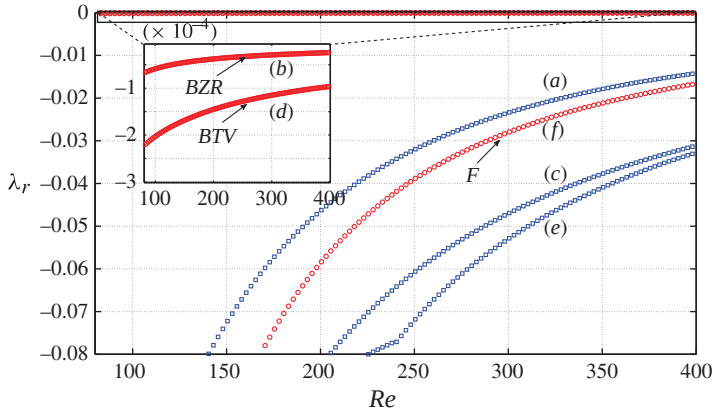

FIGURE 13. (Colour online) Growth rates of the steady axisymmetric modes of a disk with $\chi = \infty$. The squares (shown in blue online) and circles (shown in red online) respectively correspond to inertia ratios $I^* = 4 \times 10^{-3}$ and $I^* = 5 \times 10^{1}$. The inset is a zoom in the vertical direction of the almost neutral modes found in the limit $I^* \to \infty$. Symbols (a)–(f) attached to each curve correspond to those of the snapshots in figure 14. Labels *F*, *BTV* and *BZR* attached to the three branches corresponding to $I^* = 5 \times 10^{1}$ respectively refer to 'fluid', 'back-to-terminal velocity' and 'back-to-zero rotation rate' for reasons explained in the text.

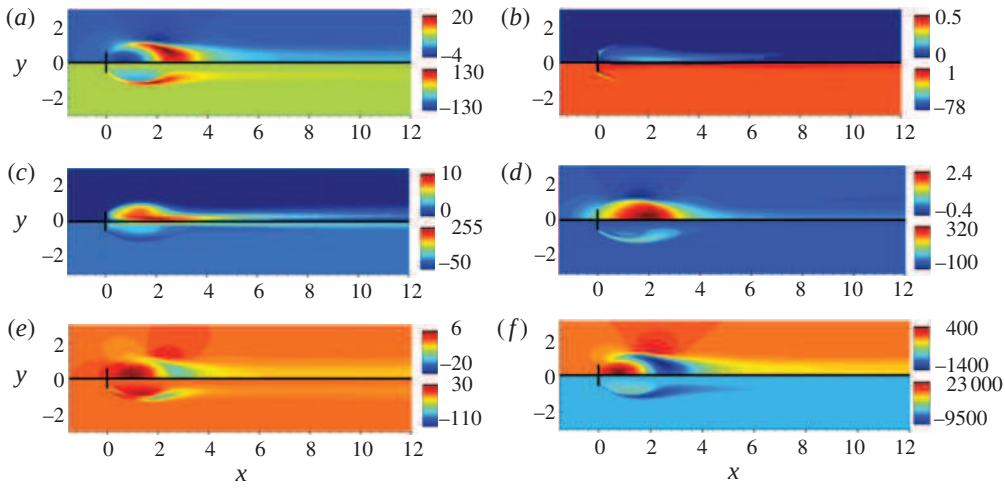

FIGURE 14. (Colour online) Axisymmetric modes of an infinitely thin disk at $Re = 328$ for $I^* = 4 \times 10^{-3}$ (left) and $I^* = 5 \times 10^{1}$ (right). For both values of I^*, the stability of the global mode increases from top to bottom. Modes (a,d,e,f) belong to the U_{RX} family and are normalized such that $\hat{u}_x = 1$, while those in (b,c) belong to the U_P family and are normalized such that $\hat{\omega}_x = 1$. For U_{RX} (respectively U_P) modes, the upper half of each snapshot displays the axial (respectively azimuthal) velocity while the lower half displays the azimuthal (respectively axial) vorticity.

relationship (D 2). The mode displayed in the snapshot in figure 14(d) was also observed with two-dimensional plates and rods by Fabre *et al.* (2011). It was termed

'back-to-terminal-velocity' (*BTV*) because it tends to dampen any perturbation that changes the relative velocity between the body and fluid in the base flow. For a similar reason, the mode displayed in the snapshot in figure 14(*b*) which is of U_P type can be termed 'back-to-zero-rotation rate' (*BZR*). These two terminologies are used in the inset of figure 13 where the growth rate of the corresponding modes is shown. While past studies tend to ignore the role of axisymmetric modes in the dynamics of bluff bodies wakes, the *BTV* and *BZR* modes reported here deserve some attention. Indeed, being very weakly damped, they may influence the nonlinear evolution of the system by interacting with the unstable low-frequency F_1 mode. At low inertia ratios, the distinction between 'fluid' and 'solid' (or 'aerodynamic') modes generally makes no sense. At first glance the structure of the mode displayed in the snapshot in figure 14(*a*) looks very similar to that in figure 14(*f*), suggesting that the '*F*' branch exists for all I^*. However, the mode in figure 14(*a*) cannot be considered as purely 'fluid' since the corresponding isovalues of the axial velocity and azimuthal vorticity indicate a non-negligible coupling between the fluid and the disk's degrees of freedom. The snapshots in figure 14(*c*) and (*e*) reveal spatial structures very different from those of the snapshots in figure 14(*b*) and (*d*). Hence, one has to conclude that the aforementioned *BZR* and *BTV* modes 'disappear' at low enough I^*. This is not unlikely since, according to figure 13, the two branches corresponding to the snapshots in figure 14(*c*) and (*e*) are much more damped than the branches *BTV* and *BZR* observed at large I^*.

Appendix D. Summary of the QST

The QST presented by Fabre *et al.* (2011) was derived through a rigourous asymptotic expansion to predict analytically the instability characteristics of a freely falling two-dimensional body in the limit of large solid-to-fluid density ratios. It is mainly based on the idea that in this limit an unsteady body motion happens on a time scale much larger than those governing the flow dynamics. This assumption allows the so-called 'aerodynamic' modes tied to the body to be computed with the flow considered quasi-steady. Since the present problem with $|m| = 1$ can be reduced to an almost two-dimensional problem by using the $U(1)$ coordinates, the two-dimensional QST formulation still holds. Therefore, equation (15) from Fabre *et al.* (2011) may be applied and the most unstable eigenvalue reads at criticality

$$\lambda^{LF} = \frac{1}{2I^*}\left(\frac{\mathscr{L}_{,\alpha}}{16} + \mathscr{M}_{,\omega}\right) \pm \sqrt{\frac{\mathscr{M}_{,\alpha}}{I^*}}, \tag{D 1}$$

where *LF* stands for 'low frequency', $\mathscr{L}_{,\alpha}$ (respectively $\mathscr{M}_{,\alpha}$) denotes the lift force (respectively torque) due to a change in the incidence angle (defined as the angle between the disk translational velocity and its symmetry axis) and $\mathscr{M}_{,\omega}$ denotes the torque induced by a weak rotation of the disk about one of its diameters. These coefficients can be computed by solving a series of elementary problems, following the procedure described by Fabre *et al.* (2011) for two-dimensional bodies.

When the right-hand side of (D 1) is complex (i.e. $\mathscr{M}_{,\alpha}$ is negative), searching for the value of *Ar* at which the real part vanishes provides the corresponding threshold; note that this threshold does not depend on I^*. Fabre *et al.* (2011) showed that such a threshold exists for two-dimensional square rods above $Re = 48$, yielding the onset of an unstable oscillating mode characterized by a strong coupling between the body and its wake. A more thorough study of the QST for three-dimensional bodies will

be the subject of a future paper. Here, it is enough to say that the S_1 mode observed in the present study for the three aspect ratios we considered is the counterpart of the mode observed for the aforementioned square rod, and that the conclusions of the two-dimensional study regarding this mode are globally applicable here. However, a central difference in the compared behaviour of two- and three-dimensional bodies must be pointed out: in the limit of large inertia ratios, we found the 'solid' S_1 mode to be more unstable than the 'fluid' modes for disks, while in the case of the square rod the former was found to be slightly less unstable than the latter (namely, the classical von Kármán shedding mode which emerges at $Re \approx 44$).

Finally, let us mention that the QST also predicts an antisymmetric 'back-to-vertical' (*BV*) and an axisymmetric 'back-to-terminal-velocity' (*BTV*) stationary mode whose growth rates may be shown to be always negative. As discussed in appendix C, in the present three-dimensional case there is also an axisymmetric 'back-to-zero-rotation rate' (*BZR*) global mode which is stationary and stable. The growth rates of these last two damped modes are

$$\lambda^{BTV} = -\frac{\mathscr{D}_{,u}}{16I^{**}}, \quad \lambda^{BZR} = -\frac{\mathscr{M}^x_{,\omega}}{2I^{**}}, \tag{D 2}$$

where $\mathscr{D}_{,u}$ stands for the drag variation due a change in the body velocity, $\mathscr{M}^x_{,\omega}$ denotes the axial torque due to a weak rotation about the disk axis, and again $I^{**} = I^*(1 + (4/3)\chi^{-2})^{-1}$.

REFERENCES

ALBEN, S. 2008 An implicit method for coupled flow–body dynamics. *J. Comput. Phys.* **227**, 4912–4933.

ASSEMAT, P., FABRE, D. & MAGNAUDET, J. 2012 The onset of unsteadiness of two-dimensional bodies falling or rising freely in a viscous fluid: a linear study. *J. Fluid Mech.* **690**, 173–202.

AUGUSTE, F. 2010 Instabilités de sillage générées derrière un corps solide cylindrique fixe ou mobile dans un fluide visqueux. PhD thesis, Université de Toulouse, Toulouse, France. Available at http://thesesups.ups-tlse.fr/1186/.

AUGUSTE, F., MAGNAUDET, J. & FABRE, D. 2013 Falling styles of disks. *J. Fluid Mech.* **719**, 388–405.

CHRUST, M., BOUCHET, G. & DUSEK, J. 2013 Numerical simulation of the dynamics of freely falling discs. *Phys. Fluids* **25**, 044102.

ERN, P., RISSO, F., FABRE, D. & MAGNAUDET, J. 2012 Wake-induced oscillatory paths of bodies freely rising or falling in fluids. *Annu. Rev. Fluid Mech.* **44**, 97–121.

FABRE, D., ASSEMAT, P. & MAGNAUDET, J. 2011 A quasi-static approach to the stability of the path of heavy bodies falling within a viscous fluid. *J. Fluids Struct.* **27**, 758–767.

FABRE, D., TCHOUFAG, J. & MAGNAUDET, J. 2012 The steady oblique path of buoyancy-driven disks and spheres. *J. Fluid Mech.* **707**, 24–36.

FERNANDES, P. C., ERN, P., RISSO, F. & MAGNAUDET, J. 2008 Dynamics of axisymmetric bodies rising along a zigzag path. *J. Fluid Mech.* **606**, 209–223.

FERNANDES, P. C., RISSO, F., ERN, P. & MAGNAUDET, J. 2007 Oscillatory motion and wake instability of freely-rising axisymmetric bodies. *J. Fluid Mech.* **573**, 479–502.

FIELD, S. B., KLAUS, M., MOORE, M. G. & NORI, F. 1997 Chaotic dynamics of falling disks. *Nature* **388**, 252–254.

HOROWITZ, M. & WILLIAMSON, C. H. K. 2010 The effect of Reynolds number on the dynamics and wakes of freely rising and falling spheres. *J. Fluid Mech.* **651**, 251–294.

HOWE, M. S. 1995 On the force and moment on a body in an incompressible fluid, with application to rigid bodies and bubbles at high and low Reynolds numbers. *Q. J. Mech. Appl. Maths* **48**, 401–426.

JENNY, M. & DUSEK, J. 2004 Efficient numerical method for the direct numerical simulation of the flow past a single light moving spherical body in transitional regimes. *J. Comput. Phys.* **194**, 215–232.

JENNY, M., DUSEK, J. & BOUCHET, G. 2004 Instabilities and transition of a sphere falling or ascending freely in a Newtonian fluid. *J. Fluid Mech.* **508**, 201–239.

MAGNAUDET, J. 2011 A 'reciprocal' theorem for the prediction of loads on a body moving in an inhomogeneous flow at arbitrary Reynolds number. *J. Fluid Mech.* **689**, 564–604.

MELIGA, P., CHOMAZ, J. M. & SIPP, D. 2009*a* Global mode interaction and pattern selection in the wake of a disk: a weakly nonlinear expansion. *J. Fluid Mech.* **633**, 159–189.

MELIGA, P., CHOMAZ, J. M. & SIPP, D. 2009*b* Unsteadiness in the wake of disks and spheres: instability, receptivity and control using direct and adjoint global stability analyses. *J. Fluids Struct.* **25**, 601–616.

MOUGIN, G. & MAGNAUDET, J. 2002*a* The generalized Kirchhoff equations and their application to the interaction between a rigid body and a arbitrary time-dependent viscous flow. *Intl J. Multiphase Flow* **28**, 1837–1851.

MOUGIN, G. & MAGNAUDET, J. 2002*b* Path instability of a rising bubble. *Phys. Rev. Lett.* **88**, 014502.

NATARAJAN, R. & ACRIVOS, A. 1993 The instability of the steady flow past spheres and disks. *J. Fluid Mech.* **254**, 323–344.

PROSPERETTI, A. 2004 Bubbles. *Phys. Fluids* **16**, 1852–1865.

PROSPERETTI, A., OHL, C. D., TIJINK, A., MOUGIN, G. & MAGNAUDET, J. 2003 Leonardo's paradox (Appendix to 'The added mass of an expanding bubble' by C. D. Ohl, A. Tijink and A. Prosperetti). *J. Fluid Mech.* **482**, 271–290.

ROOS, F. & WILLMARTH, W. 1971 Some experimental results on sphere and disk drag. *AIAA J.* **9**, 285–291.

TCHOUFAG, J., MAGNAUDET, J. & FABRE, D. 2013 Linear stability and sensitivity of the flow past a fixed oblate spheroidal bubble. *Phys. Fluids* **25**, 054108.

VELDHUIS, C. H. J. & BIESHEUVEL, A. 2007 An experimental study of the regimes of motion of spheres falling or ascending freely in a Newtonian fluid. *Intl J. Multiphase Flow* **33**, 1074–1087.

WILLMARTH, W., HAWK, N. & HARVEY, R. 1964 Steady and unsteady motions and wakes of freely falling disks. *Phys. Fluids* **7**, 197–208.